

## Master Thesis

Development, Implementation and Validation of a Software  
Defined Radio Spectrometer and its Application in Magnetic  
Resonance at Low Magnetic Field Strengths ( $B_0=0.08 - 0.3T$ )

30th of November 2016

Submitted by:

Christian Blücher, B.Sc.

Matriculation Number: 1780636

bluecher.christian@outlook.com

Institute of Biomedical Engineering  
Karlsruhe Institute of Technology (KIT)  
Karlsruhe, Germany  
Supervisor: Prof. Dr. Olaf Dössel

Berlin Ultrahigh Field Facility (B.U.F.F.)  
Max Delbrück Center for Molecular Medicine  
Berlin, Germany  
Supervisors: Dr. Lukas Winter  
Prof. Dr. Thoralf Niendorf

**Eidesstattliche Erklärung:**

Ich versichere wahrheitsgemäß, die Arbeit selbstständig angefertigt, alle benutzten Hilfsmittel vollständig und genau angegeben und alles kenntlich gemacht zu haben, was aus Arbeiten anderer unverändert oder mit Abänderungen entnommen wurde.

Karlsruhe, den 30. November 2016

---

Unterschrift

# Acknowledgments

I would like to thank my supervisor at the Berlin Ultra High Field facility (B.U.F.F.), Dr. Lukas Winter, for his helpful guidance and great supervision throughout the course of my thesis. He provided me with continuous support and encouragement, especially in times when I needed it the most. Furthermore, I would like to thank the whole B.U.F.F. team for their warm welcome, fun lunch and coffee breaks and helpful comments and suggestion. In particular, I would like to thank Prof. Thoralf Niendorf for giving me the opportunity to be part of such an interesting project and great research team.

In addition, I would like to thank Werner Hoffman and Reiner Seemann (PTB) for their patient help and support with the not always nicely behaving RF-Power Amplifier and Frank Seifert (PTB) for his support with the TEM cell measurements.

Finally, I would like to thank Prof. Olaf Dössel from the Karlsruhe Institute of Technology for supervising and supporting me as an external master student.

# Abstract

Magnetic resonance imaging (MRI) is the most powerful diagnostic imaging modality available today and key to an early diagnosis and successful treatment of many diseases and injuries. Its major drawbacks are cost and complexity, limiting its use largely to industrialized countries and large hospitals, excluding many patients around the world from the benefits of this crucial medical device.

In order to address this issue, cost effective open source imaging (COSI) which is part of the open source imaging initiative (OSI<sup>2</sup>) is currently building an affordable open source MR scanner. In this master thesis, a MR transmission reception radio frequency (RF) system for traditional and rotating spatial encoding schemes was developed. The implemented system is based on a GNU Radio compatible software defined radio (SDR) as a spectrometer, a custom made RF power amplifier (RFPA), a transmit/receive switch, a low noise preamplifier and a transmit/receive solenoid RF coil. In its current configuration it is compatible to a Halbach prototype magnet ( $B_0=0.085\text{T}$ ) with a rotating gradient system which is currently being constructed.

Results show that the spectrometer is capable of producing arbitrary shaped RF pulses and recording the acquired MR-signal in a user defined time window. The custom made RFPA successfully amplifies the generated RF pulses and provides a maximum output power of 1kW. This allows for a total  $B_1^+$  amplitude of  $2694\mu\text{T}$  generated by the designed and constructed transmit/receive RF coil at  $f=3.63\text{MHz}$  ( $B_0=0.085\text{T}$ ). In its current configuration the system can be used in the frequency range  $f=1.8\text{--}30\text{MHz}$  ( $B_0=0.042\text{T--}0.7\text{T}$ ). It consist of mostly open source software and hardware components and the total costs are less than 3000€. The modular system structure provides a firm basis for future research and developments and allows using the individual system parts in the context of other projects.

# Table of Contents

Acknowledgments .....	I
Abstract .....	II
Table of Contents.....	III
List of Figures.....	V
Abbreviations .....	VIII
1. Introduction .....	1
2. Theoretical Concepts.....	3
2.1 The Principles of Magnetic Resonance Imaging.....	3
2.1.1 The Nuclear Magnetic Resonance (NMR) Phenomenon.....	3
2.1.2 Excitation Pulse and Signal Detection .....	5
2.1.3 Relaxation Times.....	6
2.1.4 Basics of Imaging .....	7
2.2 Components of an MRI Scanner .....	8
3. Materials and Methods .....	11
3.1 Structure of COSY MR-System .....	11
3.2 The Spectrometer .....	13
3.2.1 Spectrometer Hardware .....	13
3.2.2 Software Defined Radio (SDR) Spectrometer .....	14
3.3 The RF Power Amplifier .....	20
3.4 The Transmit/Receive-Switch .....	23
3.5 The NMR Signal Preamplifier .....	24
3.6 The RF Coil.....	25
3.6.1 Basics.....	25
3.6.2 The RF Coil Design.....	27
3.6.3 Electromagnetic Field Simulations.....	28
3.6.4 $B_1^+$ Field Validation Measurements .....	29

4.	Results .....	31
4.1	Results SDR Spectrometer .....	31
4.2	Results RFPA.....	34
4.2.1	Output Signal Level Converter.....	34
4.2.2	Input Power vs. Output Power .....	35
4.2.3	Amplified RF Pulses.....	36
4.3	Results Solenoid RF Coil .....	37
4.3.1	$B_1^+$ Field Simulations .....	37
4.3.2	Construction .....	40
4.3.3	Bench Measurement.....	41
4.3.4	Measured $B_1^+$ Field.....	41
4.3.5	Comparison of Measured and Simulated $B_1^+$ Field .....	43
4.4	Complete MR Transmission/Reception System .....	44
5.	Discussion and Conclusion.....	45
	References.....	48
	Appendix .....	51

# List of Figures

Figure 1: Magnetic moment of a charged sphere, where each charged particle contributes to the magnetic moment [Adaption from [23]].....	3
Figure 2: Nuclear Zeeman levels of a nucleus with a spin of $I = 1/2$ (e.g. hydrogen nucleus) [Adaption from [23]] .....	4
Figure 3: a) Precession cone for nucleus with a nuclear spin of $I=0,5$ , allowing only two discrete spin states; b) Origin of macroscopic magnetization $M_0$ due to the difference in the occupation numbers of the two energy levels [Adaption from [23]] .....	5
Figure 4: Precession of magnetization vector along the direction of the external field $B_0$ due to the presence of a with the Larmor frequency alternating electromagnetic field $B_1$ [Adaption from [23]] ...	6
Figure 5: a) The longitudinal magnetization $M_z$ relaxes towards the equilibrium value $M_0$ after $90^\circ$ pulse. b) The transversal magnetization $M_{xy}$ decreases towards zero after a $90^\circ$ pulse. [Adaption from [23]]	7
Figure 6: Diagram of a spin echo sequence as example for the timing of the RF excitation pulse, the gradient pulses and the acquisition window of an imaging technique. ....	8
Figure 7: Schematic of the key components of an MRI Scanner. ....	9
Figure 8: a) 3D model of the dipole Halbach magnet and the quadrupolar Halbach gradient ring constructed from small, octagonal shaped permanent magnets ( $B_r=1.42$ ). b) Illustration of the arrangement of the single permanent magnets in a dipole Halbach arrangement on a circle and the resulting magnetic field distribution.....	11
Figure 9: The two orthogonal gradient fields of a quadrupolar Halbach magnet ring. ....	12
Figure 10: Schematic of the implemented COSY MR-system.....	12
Figure 11: USRP1 motherboard from Ettus Research equipped with one receive LFRX daughterboard and two transmit LFTX daughterboards. ....	16
Figure 12: Schematic of the implemented SDR spectrometer. ....	18
Figure 13: Schematic of the implemented GNU Radio Flowgraph for the MR spectrometer. ....	19
Figure 14: Schematic of the implemented RFPA with 1kW output peak power and a frequency range from 1.8-54MHz.....	21
Figure 15: The graph shows the beginning and the end of unblanking pulse of the RFPA (green) and the corresponding course of the 50V power supply voltage of the final amplification stage (blue) prior to removing the RF blocking capacitors. ....	22
Figure 16: The graph shows the beginning and the end of unblanking pulse of the RFPA (green) and the corresponding course of the 50V power supply voltage of the final amplification stage (blue) after the RF blocking capacitors were removed and put behind the switching transistor. ....	22

Figure 17: a) Circuit diagram of the implemented level converter to convert the amplitude of the RFPA unblanking pulse from 1V – produced by the spectrometer – to TTL level. b) Picture of the Level Converter. ....	23
Figure 18: Passive T/R-switch produced by the company NMR Service GmbH (Erfurt, Germany). ....	24
Figure 19: Photograph of the LNA4HF which is used as preamplifier. It covers a frequency range of 150 kHz – 30 MHz and provides a gain of 18-20 dB and a N.F. of 1-2dB. ....	25
Figure 20: Series RLC resonance circuit with capacitive tuning-matching circuit. ....	27
Figure 21: CST simulation model of solenoid RF coil (yellow) and spherical sample (green). ....	28
Figure 22: Photograph of the $B_1^+$ field measurement setup for the constructed solenoid coil with a pickup loop positioned along the measurement path. ....	29
Figure 23: Left side: Transverse ElectroMagnetic (TEM) Cell used for the calibration of the pickup loop. Right side: Pickup loop inside of TEM cell for calibration. ....	30
Figure 24: The graphs shows the measured signals produced by the spectrometer when a rect-pulse with an amplitude of 500mV and a length of 200 $\mu$ s, a readout delay of 80 $\mu$ s and a readout length of 500 $\mu$ s was specified in the software. ....	31
Figure 25: The graph shows a detailed enlargement of the measured rect-pulses generated by the Spectrometer. ....	31
Figure 26: a) The graph shows a measured sinc-pulse with a maximum amplitude of 200mV and a length of 120 $\mu$ s generated by the spectrometer as an example for a more complexed shaped RF-pulse. b) Shows the digital representation of the generated sinc-pulse. ....	32
Figure 27: The graph shows 3 pulses produced at the GPIO pins of the LFTX B daughterboard of the spectrometer which are used to control the stepper motor for the gradient ring rotation. The 3 shown positive pulses edges would turn the stepper motor by three angle steps. ....	33
Figure 28: Three Screenshots of the SDR spectrometer GUI displaying the received signals for different test signals in order to mimic the NMR signal at the spectrometer input. The spectrometer was set to a Larmor frequency of 3.63MHz. The test signals were: a) $f=3.63\text{MHz}$ $P=-40\text{dBm}$ , b) $f=3.632\text{MHz}$ $P=-40\text{dBm}$ and c) $f=3.632\text{MHz}$ $P=-40\text{dBm}$ . For the measurement in c) the preamplifier had been removed. ....	34
Figure 29: The graph shows the unblanking pulse for the RFPA as it is produced by the spectrometer (blue curve) and after it has passed the level converter (green curve). The amplitude is raised from 1V to 3V by the level converter. ....	35
Figure 30: Input power $P_{\text{in}}$ plot versus the output power $P_{\text{out}}$ of the RFPA for the Larmor frequencies of hydrogen at magnetic field strengths $B_0= 0.1\text{T}$ , $0.2\text{T}$ , $0.3\text{T}$ , $0.5\text{T}$ and $1.0\text{T}$ showing good linearity over the investigated frequency range. ....	35



Figure 31: A 1200 $\mu$ s long rect-pulse with an amplitude of 500mV (a) and a 120 $\mu$ s long sinc pulse with a maximum amplitude of 200mV (c) are shown on the left side. Both pulses are generated by the SDR spectrometer. On the right side (b,d) the same pulses are shown after amplification with the RFPA and 40dB attenuation. ....	37
Figure 32: Vector field of H-field (a) and E-field (b) (same phase) of the final solenoid RF coil design (L=200mm, N=20). ....	38
Figure 33: The graphs show the magnitude of the simulated $B_1^+$ field distribution in the transversal plane (zy-plane) of the RF coil for the parameter combinations L=160mm, N=16 (a), L=200mm, N=16 (b) and L=200mm, N=20 (c). ....	39
Figure 34: The graph shows the $B_1^+$ field values inside the sample along straight lines through the coil center in the x-, y- and z-direction respectively. ....	40
Figure 35: a) Picture of the finished solenoid RF coil (length 200 mm, number of turns 20) wound on a 3D printed cylinder. b) Picture of the tuning and matching circuit. ....	40
Figure 36: $S_{11}$ reflection measurement of solenoid coil for unloaded (a) and loaded (b) case. ....	41
Figure 37: colored curves: $S_{12}$ measurements between the solenoid coil and the pickup loop; black curve: $s_{21}$ measurement between pickup loop and TEM cell for calibration of pickup loop. ....	42
Figure 38: Measured $B_1^+$ field values generated by the solenoid RF coil along a straight line at one end of the RF coil. ....	43
Figure 39: a) Comparison of absolute values between measured and simulated $B_1$ field of solenoid coil. b) Comparison of the maximum normalized values between measured and simulated $B_1$ field of solenoid coil. ....	43
Figure 40: Photograph of the complete MR transmission and reception system consisting of the SDR spectrometer (USRP1), the RFPA, the transmit/receive RF coil, the T/R switch and the preamplifier. ....	44

# Abbreviations

ADC	Analog Digital Converter
AWG	American Wire Gauge
BNC	Bayonet Neill–Concelman
CAT	Computer-Assisted Translation
COSI	Costeffective Open Source Imaging
CST	Computer Simulation Technology
DAC	Digital Analog Converter
DDC	Digital Down Converter
DDS	Direct Digital Synthesizer
DSP	Digital Signal Processor
DUC	Digital up Converter
FID	Free Induction Decay
FPGA	Field Programmable Gate Array
GPIO	General Purpose Input Output
MR	Magnetic Resonance
MRI	Magnetic Resonance Imaging
NMR	Nuclear Magnetic Resonance
PC	Personal Computer
Q-Factor	Quality Factor
RF	Radio Frequency
RX	Receive
SDR	Software Defined Radio
SMA	Sub-Miniature-A
SNR	Signal to Noise Ratio
T/R-switch	Transmit/Receive Switch
TEM-cell	Transversal ElectroMagnetic Cell
TX	Transmit

# 1. Introduction

Magnetic resonance imaging (MRI) has been used for the first time to diagnose cancer in a human being in 1978 [1]. A few years later – in the early 1980s – MRI was introduced to clinical practice [2]. By now, it is the most powerful diagnostic imaging modality available and key to an early diagnosis and successful treatment of many diseases and injuries. It provides not only outstanding high soft-tissue contrast but also the possibility to non-invasively determine various physical and physiological processes inside the human body such as diffusion, perfusion, tissue oxygenation and characterization, blood flow or temperature. Furthermore and in contrast to computed tomography, the patient is not exposed to ionizing radiation. Alongside these numerous advantages two major drawbacks of the technology are the cost and complexity of current MR scanners. In particular, the use of superconducting magnets to create magnetic field strengths in the order of  $B_0 \geq 1.5\text{T}$  and a complex gradient system make MRI an extremely expensive technology. Prices range from 1.0-2.5 million euro for a clinical ( $B_0=1.5\text{T}-3.0\text{T}$ ) MR scanner followed by high service and operational costs [3, 4]. As a consequence, access to MRI is primarily restricted to industrialized countries, excluding many patients around the world from the benefits of this crucial medical device [5].

The open source imaging initiative (OSI<sup>2</sup>) ([www.opensourceimaging.org](http://www.opensourceimaging.org)) [4, 6] has the aim to approach this inequality by making MRI more accessible to researchers, developers and patients. Combining innovation and open collaboration has the potential to lower costs of acquisition, maintenance and operation of MR scanners. As part of the initiative a costeffective open source imaging (COSI) scanner is developed with its technical documentation freely available according to the standards of open source. The COSI MR-system aims at a magnetic field strength of  $B_0=0.2\text{T}$ , which is sufficiently high for a broad range of clinical applications [7-15]. Such field strengths can be achieved using permanent magnets in Halbach arrangements which tremendously reduces manufacturing and maintenance costs, allows for the construction of lighter magnets (weight  $\leq 100\text{kg}$ ) and safer operation in comparison to higher field systems [16]. Further, the complex gradient system of a conventional scanner can be replaced by a rotating gradient system with permanent magnets, avoiding costly gradient amplifiers and enabling “silent” spatial encoding [17]. In contrast to rotating the whole magnet [17], the concept involves a homogeneous Halbach magnet design at  $B_0=0.2\text{T}$  that is superimposed by a much lighter rotating Halbach gradient ring of lower field strengths [16, 18]. Moreover, a custom made MR transmission/reception system is required since commercially available systems are too expensive, do not provide an interface for gradient field rotation and cannot be adapted due to their non-open-source nature [19-21].

Within this framework, in this master thesis a suitable transmission and reception system was developed and implemented. The modular system consists of a spectrometer, RF power amplifier, transmit/receive switch, RF coil and low noise preamplifier with the results of this work being made available by the standards of open source.

In the following, the theoretical concept of MRI and the composition of a traditional MRI scanner are introduced. In the main part, the general structure of the implemented low-field MRI system and its individual components are outlined and explained in detail. Existing concepts from the literature are reviewed and benchmarked against the finally pursued implementation. Finally, the functionality of the constructed components is demonstrated and the results are discussed.

## 2. Theoretical Concepts

### 2.1 The Principles of Magnetic Resonance Imaging

Magnetic resonance imaging (MRI) is an imaging modality used in clinical diagnostics to acquire images of the anatomy of the human body and to visualize physiological processes. Its ability to produce images with great soft tissue contrast and its flexibility to create images of slices in arbitrary orientation has made MRI to the number one choice in many diagnostic questions in daily clinical routine [2]. In this chapter the basics of this powerful method are explained.

#### 2.1.1 The Nuclear Magnetic Resonance (NMR) Phenomenon

MRI is based upon the interaction of nuclear spins with an external magnetic field  $B_0$  [22] and utilizes the fact that ensembles of these spins can be “controlled” with radio frequency signals.

All atomic nuclei with an odd number of nucleons possess an intrinsic angular momentum or nuclear spin  $I$ . Such a spin  $I$  is always related to a nuclear magnetic moment  $\mu$  according to the following equation:

$$\mu = \gamma * I \quad (1)$$

Therein,  $\gamma$  is a proportionality constant, the so called gyromagnetic ratio, which is characteristic for each specific nucleus. A nucleus can be thought of as a rotating, charged sphere – as depicted in Figure 1 – where each charged particle contributes to the nuclear magnetic moment  $\mu$  [23, 24].

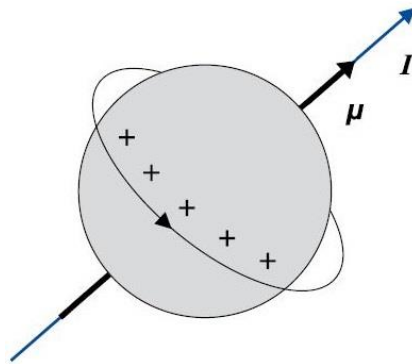


Figure 1: Magnetic moment of a charged sphere, where each charged particle contributes to the magnetic moment [Adaption from [23]].

In principal all nuclei with a spin unequal to zero can be utilized in MRI. In practice usually the hydrogen proton  $H^1$  is used since it is the most abundant element in biological tissue and has the largest gyromagnetic ratio ( $\gamma/2\pi = 42.576 \text{ MHz/T}$ ) and thus the greatest magnetic moment. Without any external magnetic field being present, the energy levels of all particles with a magnetic moment are the same (see Figure 2 left side). However, when a homogenous magnetic field with the flux density

$B_0$  is applied, the magnetic moments align to the external field and gain additional potential energy (see Figure 2 right side). According to the laws of quantum mechanics, only  $2I+1$  discrete and equidistant energy levels are allowed, given by [2, 23]:

$$E_m = -\gamma * \hbar * B_0 * m \quad (2),$$

where  $\hbar$  is the reduced Planck's constant ( $\hbar = h/2\pi = 1.055 \cdot 10^{-34} \text{ Ws}^2$ ) and  $m$  the magnetic quantum number ( $-I \leq m \leq I$ ). These discrete energy levels are referred to as Zeeman levels. For hydrogen (Spin  $I=1/2$ ) there are two different energy levels - as depicted in Figure 2 - where on the lower level spins are aligned parallel (spin-up orientation) and on the higher level antiparallel (spin-down orientation) with respect to the external field  $B_0$  [23].

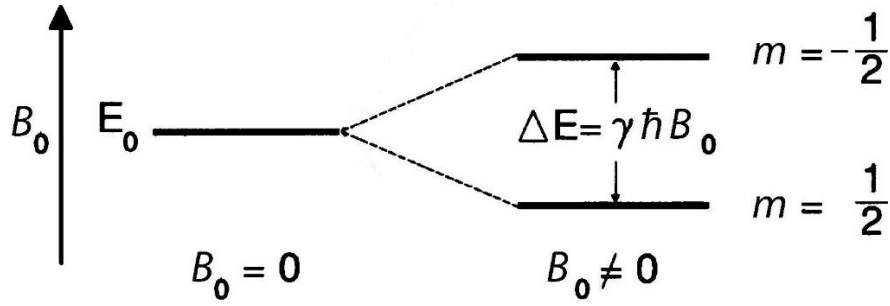


Figure 2: Nuclear Zeeman levels of a nucleus with a spin of  $I = 1/2$  (e.g. hydrogen nucleus) [Adaption from [23]]

In thermal equilibrium, the overall occupation of the different energy levels is given by the Boltzmann distribution:

$$\frac{N_{\uparrow}}{N_{\downarrow}} = e^{\frac{\Delta E}{k_b * T}} \quad (3)$$

Where  $k_b$  is the Boltzmann's constant ( $1,38 \cdot 10^{-23} \text{ Ws/K}$ ),  $T$  the sample temperature in Kelvin,  $\Delta E$  the energy difference between two levels and  $N_{\uparrow}$  and  $N_{\downarrow}$  are the numbers of spins on the lower and upper level respectively. The lower energy level is slightly favored so that there are more spins aligned parallel to the external field than there are antiparallel. This leads to a macroscopic magnetization vector  $M_0$  in the direction of the external magnetic field [2, 24].

A transition between the different levels is only possible via an energy exchange in form of a photon loss or gain where the energy of the photon  $E_{\text{photon}} = \hbar * \omega_{\text{photon}}$  equals the energy difference  $\Delta E = \gamma * \hbar * B_0$  between the levels [2, 23]. This yields to a resonance condition which is described by the well know Larmor equation:

$$\omega_{\text{Lamor}} = \gamma * B_0 \quad (4)$$

$\omega_{\text{Larmor}}$  is the frequency a photon must have in order to induce a transition between two adjacent energy levels. In MRI this is achieved by a radio frequency pulse (RF-pulse) at the Larmor frequency which is transmitted perpendicular to the direction of the static magnetic field  $B_0$  [23].

The basics of MRI/NMR can also be explained with a semi-classical approach where a nucleus can be imagined as a rotating, charged sphere as described earlier. In a magnetic field free environment the magnetic moments of the nuclei are randomly oriented in space and thus the overall magnetization is zero. However, when placed in an external magnetic field  $B_0$  the magnetic moments experience a torque which leads to their precession around the axis of the external field. The frequency of this rotation is again described by the Larmor frequency as defined in equation (4). Also the quantization of direction of the magnetic moments can be included into this classical model by only allowing certain, discrete angles between the field's axis and the precession cone (see Figure 3a)) [23]. All nuclei with the same gyromagnetic ratio will precess with the same characteristic Larmor frequency but will not have the same phasing so that the individual magnetic moment vectors are uniformly spread on the precession cone. Consequently, the x and y components of the  $\mu$  vectors annihilate each other and only the z component sums up to macroscopic magnetization vector  $M_0$  along the  $B_0$ -field axis as depicted in Figure 3b) – again due to the difference in the occupation numbers of the two possible spin states [23].

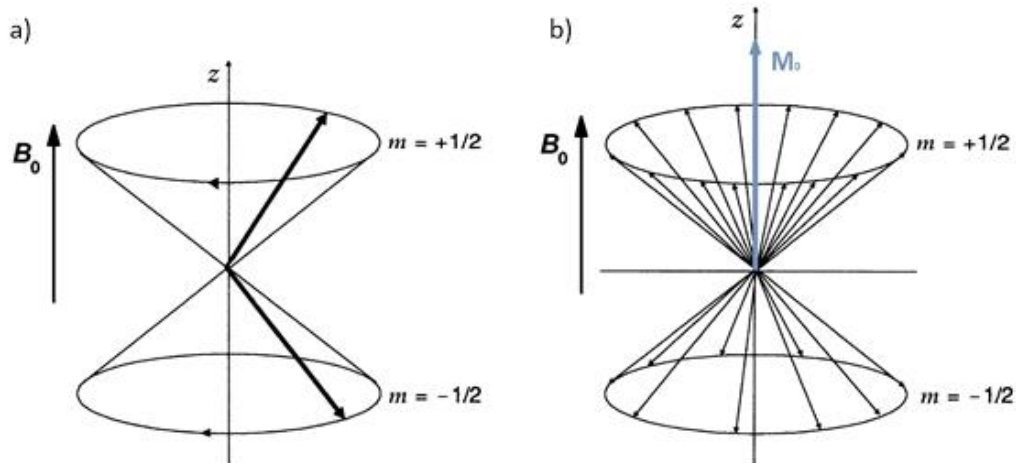


Figure 3: a) Precession cone for nucleus with a nuclear spin of  $I=1/2$ , allowing only two discrete spin states; b) Origin of macroscopic magnetization  $M_0$  due to the difference in the occupation numbers of the two energy levels [Adaption from [23]]

### 2.1.2 Excitation Pulse and Signal Detection

The state of thermal equilibrium – in which the magnetization vector  $M_0$  is pointing in the direction of the external  $B_0$  field (z-direction) – can be disturbed by the application of an alternating electromagnetic field  $B_1$  perpendicular to the external field (transversal direction). Thereby, the alternation frequency of the  $B_1$  field has to match the Larmor frequency  $\omega_{\text{Larmor}}$  of the considered

nucleus. This is referred to as radio frequency (RF) excitation pulse. The irradiation of energy at the resonance frequency elevates some spins of the lower Zeeman level to the higher level, thus reducing the difference in the occupation number. Consequently, the z-component of the magnetization decreases. Furthermore, the different precession phases of the individual spins are synchronized which leads to the formation of a magnetization component in the transversal direction. Looking from a macroscopic perspective, these processes can be described as a deflection of the magnetization vector  $M_0$  away from the  $B_0$ -direction into a precession movement around the external field axis with the Larmor frequency. Thereby the tip of  $M_0$  starts to move in a spiral on the surface of a sphere, down towards the transversal plane (the length of  $M_0$  remains constant), as depicted in Figure 4. Depending on the amplitude and the length of the excitation pulse it gets more or less deflected (e.g.  $90^\circ$  pulse or  $180^\circ$  pulse). After switching off the excitation pulse the magnetization continues to rotate. Since the magnetization vector is representing many small magnetic moments, their rotation produce an over the time varying magnetic flux density  $\Phi(t)$  in space, which – according to Faraday's law – induces an electromagnetic force in a receiver antenna. This signal oscillates with the Larmor frequency and decays in time due to relaxation processes in the sample. It is referred to as the free induction decay (FID) signal [23, 24].

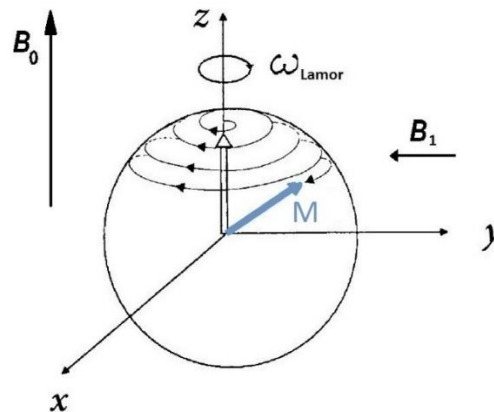


Figure 4: Precession of magnetization vector along the direction of the external field  $B_0$  due to the presence of a with the Larmor frequency alternating electromagnetic field  $B_1$  [Adaption from [23]]

### 2.1.3 Relaxation Times

Under ideal conditions, the excited magnetization vector would continue to precess as manipulated by the RF excitation pulse forever. However, in MR the interaction of nuclear spins with one another and with their environment cause the magnetization to decay. These two effects – the so-called relaxation processes – can be described by exponential functions with the relaxation time constants  $T_1$  and  $T_2$ . The longitudinal relaxation time  $T_1$  defines the time required – after a  $90^\circ$  pulse – for the longitudinal magnetization component  $M_z$  to reach 63% of its initial value  $M_0$ , as shown in Figure 5a). This relaxation arises from the falling back of the excited spins to the lower energy level. Thereby, the



energy difference is dissipated by the surrounding environment (lattice) which is why this relaxation process is also referred to as spin-lattice relaxation. The transverse relaxation time  $T_2$  specifies the time needed until the transverse component  $M_{xy}$  of the magnetization has dropped to 37% of its original magnitude – as depicted in Figure 5b) – due to spin-spin interactions. These interferences between spins lead to slightly different rotation frequencies of the individual spins which results in a dephasing, thus reducing the transverse magnetization component. In practice, also inhomogeneity in the static magnetic field  $B_0$  induce dephasing of the spins. This can be incorporated into the transverse relaxation time and is then denoted as  $T_2^*$ . In general different biological tissue types have specific  $T_1$  and  $T_2$  values. MRI utilizes this to achieve great soft tissue contrast [23, 24].

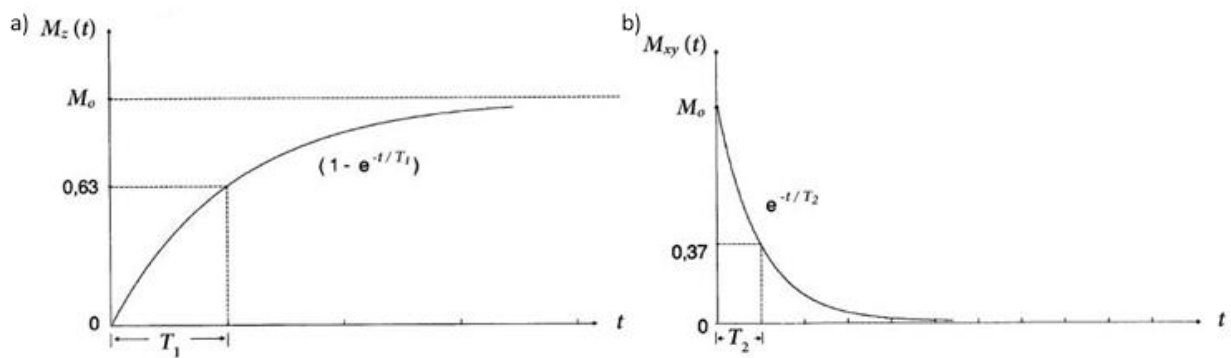


Figure 5: a) The longitudinal magnetization  $M_z$  relaxes towards the equilibrium value  $M_0$  after  $90^\circ$  pulse. b) The transversal magnetization  $M_{xy}$  decreases towards zero after a  $90^\circ$  pulse. [Adaption from [23]]

### 2.1.4 Basics of Imaging

In order to be able to reconstruct an image from the acquired NMR signal – which so far is the signal originated from the whole sample – spatial information needs to be added to the signal. This is typically achieved by three additional magnetic field gradients  $G_{x,y,z}$  in each spatial direction. The gradient fields are superimposed to the static magnetic field  $B_0$  and are switched on and off at specific time points during an imaging technique. These spatially varying encoding fields cause the Larmor frequency to vary along each direction in space. For 2D imaging, a so called slice selection gradient is turned on during the excitation pulse leading to the excitation of only one 2D slice around the center frequency. Hence, the manipulations are reduced to one slice instead of the whole sample volume. Before signal acquisition, an amplitude modulated phase encoding gradient (orthogonal to the slice encoding gradient) is switched on for a certain time causing the excited spins to rotate with different frequencies along the encoding direction. When switching the gradient off again the spins return to the original precession frequency but the developed phase difference remains. During the data acquisition window, a frequency encoding or readout gradient is turned on which leads to different rotation frequencies of the spins during the data acquisition along that gradient direction. The 2D frequency encoded data, the so called k-space, consists of k-space lines acquired at varying phase encoding

gradients (per k-space line) and fixed frequency encoding gradients. Calculating the inverse 2D Fourier transformation of the k-space image transforms frequencies into spatial information or a 2D image of the object [23, 24]. Figure 6 shows the timing of a spin echo sequence as one example of an imaging technique. The  $180^\circ$  RF pulse is required to compensate spin dephasing due to the  $T_2^*$  relaxation processes and leads to a signal echo during the acquisition window.

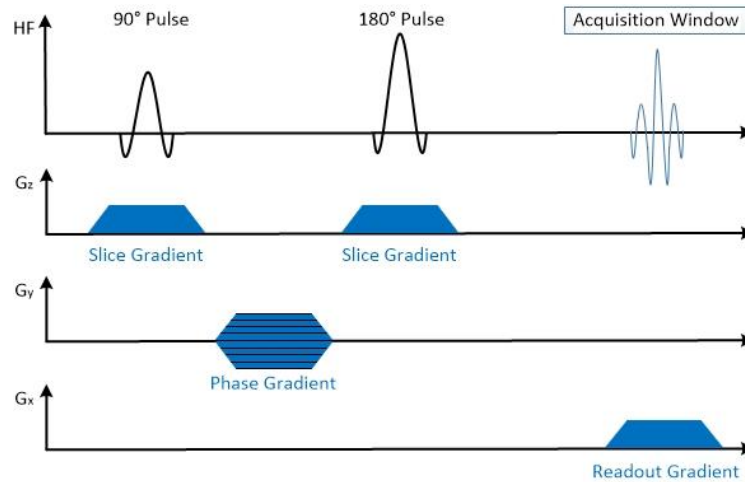


Figure 6: Diagram of a spin echo sequence as example for the timing of the RF excitation pulse, the gradient pulses and the acquisition window of an MR imaging technique.

An alternative method to retrieve an image from the acquired MR signal is the projection method introduced by Lauterbur in 1973 [25]. Thereby, a linear gradient field is rotated in relation to the object. For each rotation angle a one-dimensional projection along the gradient direction is acquired. According to the Fourier slice theorem, the 1D Fourier transformation of a projection yields the data in the Fourier transformed image along a straight line through the center of the coordinate system. In MRI the measured signal represents already the 1D Fourier transformation of a projection so that the real- and imaginary-part of the measured signal can be directly inscribed into the k-space image. 2D Fourier transformation of the k-space image forms the 2D image of the object [24].

## 2.2 Components of an MRI Scanner

An MRI scanner can be divided into four subsystems: The magnet, the gradient-system, the radio frequency (RF) system and the control-unit. A schematic of the key components of an MRI scanner is shown in Figure 7.

- The **magnet** generates the required static and homogeneous magnetic field  $B_0$  which is necessary to establish a longitudinal magnetization. Clinical systems usually use a superconducting magnet in order to reach high magnetic field strengths (typically 1.5T or 3T) and an additional shim-system to satisfy the requirements of field homogeneity [2, 23].

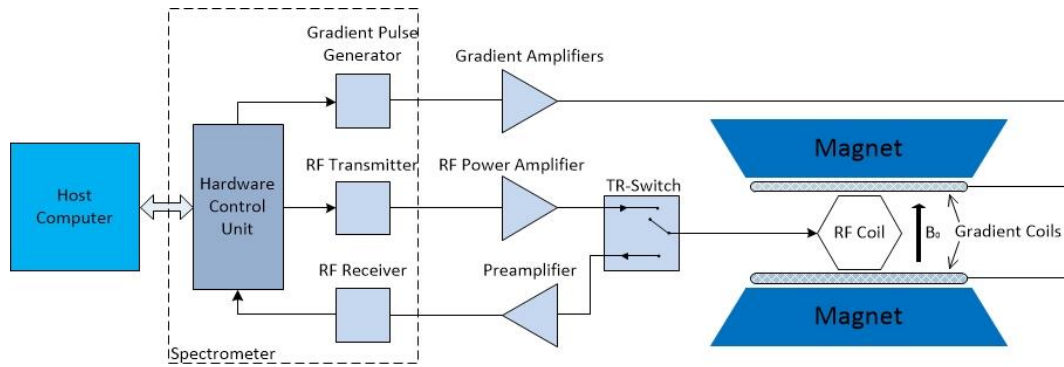


Figure 7: Schematic of the key components of an MRI Scanner.

- The **gradient-system** consist of three gradient coils, the gradient amplifiers and the gradient pulse generator. Each of the three gradient coils creates an additional linear magnetic gradient field in the x-, y- or z-direction respectively. The gradient fields can be switched on and off which allows the assignment of spatial information to the acquired MR signals. The gradient coils are driven with a current that is produced by the gradient pulse generator and amplified by the gradient amplifiers at specific points in an MR imaging technique [2, 23].
- The **RF-system** is needed to transmit an RF pulse in order to excite the nuclear spins of the tissue and to detect the weak induced MR signals received from the same tissue. Accordingly, it can be divided into the transmit path and the receive path. The former consist of the RF transmitter which produces the RF excitation pulse, the RF power amplifier which amplifies the RF pulse, the transmit/receive switch (TR switch) and the RF coil. The RF coil transmits the RF pulse as a circular polarized magnetic field  $B_1^+$  perpendicular to the direction of the main magnetic field  $B_0$ . It also acts as the receive antenna to pick up the induced MR signal  $B_1^-$ . The RF coil functions as both transmitter and receiver. While the transmit path requires high peak powers ( $\sim$ kW), the receive amplitudes are fairly low ( $\sim$ -70dBm) requiring low noise pre-amplification. In the RF receiver the signal is demodulated, split into real- and imaginary part and finally digitized. The digital data is passed to the control unit for further processing. In order to separate transmit and receive path and protect the hardware components operating in a different power range a transmit/receive (T/R) switch is needed [2, 23].
- The **control unit** consists of the hardware computer, the host computer and the image reconstruction unit. The hardware computer controls the timing and interaction between the RF transmitter, the RF receiver and the gradient system and thus ensures that the

imaging techniques containing gradient and RF pulse timings is executed properly. Altogether, those components can be summarized as the spectrometer of the MRI system. The host computer serves as interface to the operator of the MR scanner where the imaging technique can be selected, modified and initiated and the MR data is displayed after an MR scan. The measured MR data is transformed into MR images with an image reconstruction unit [2, 23].

### 3. Materials and Methods

#### 3.1 Structure of COSI MR-System

The main difference in the Costeffective Open Source Imaging (COSI) MR-system to a conventional clinical MRI (chapter 2.2) is the use of permanent magnets instead of electro magnets to create both the main magnetic field and the linear gradient fields [16-18]. The former strongly reduces investment, maintenance and operational costs of the scanner; the latter eliminates the need for powerful gradient amplifiers and complex gradient coils. Furthermore, conventional imaging methods – using slice-, phase- and frequency-gradients – are replaced with a projection method. Thereby, the linear gradient field is rotated step by step around the sample, acquiring one dimensional projections along the gradient direction for each of the rotation angels. In the following, the practical implementation of this theoretical concept is outlined.

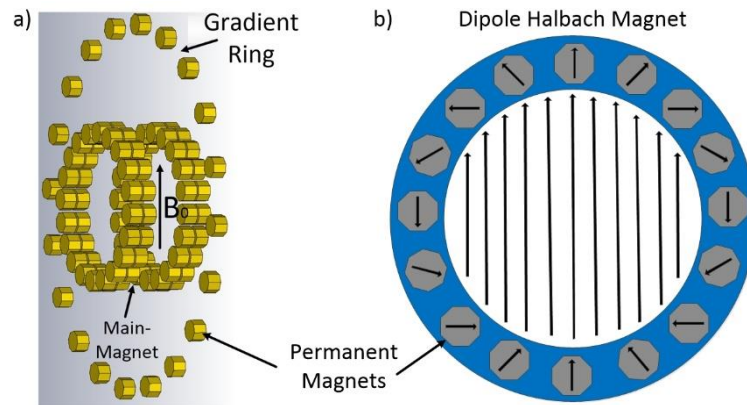


Figure 8: a) 3D model of the dipole Halbach magnet and the quadrupolar Halbach gradient ring constructed from small, octagonal shaped permanent magnets ( $B_r=1.42$ ). b) Illustration of the arrangement of the single permanent magnets in a dipole Halbach arrangement on a circle and the resulting magnetic field distribution.

To create the homogenous static magnetic field  $B_0$ , small, octagonal shaped permanent magnets in a dipole Halbach array arrangement [26] are used as it has already been done in [16, 17, 27, 28]. Two planar rings – constructed from Plexiglas and positioned on the same axis facing one another – serve as scaffolding for the magnets which are attached in a specific circular pattern to both sides of the rings. Figure 8 shows a 3D model of the construction on the left hand side and the disposal of the single magnets on a circle on the right hand side. Such a magnet design leads to a spherical relative homogeneous magnetic field in the middle of the two rings with its direction perpendicular to the axis on which the rings are positioned. The field strength in the center of the field is chosen to be approximately 85mT which corresponds to a Larmor frequency for proton of 3.63MHz.

In a similar way, the linear gradient fields required for spatial encoding are generated. Instead of a dipolar Halbach magnet a quadrupolar Halbach magnet is used as it is suggested and simulated in [16, 18]. This changes the emerging field between the two rings from a homogeneous magnetic field

(dipole) to a field with quadrupolar polarity that consists of two orthogonal and constant gradient fields. This is illustrated in Figure 9. The scaffolding-ring – in which the small permanent magnets for the gradient fields are embedded – is positioned in the middle of the two rings of the main magnet (Figure 8 a). Turning the gradient ring allows to change the direction of the gradient fields as required for the acquisition of multiple one dimensional projections along the gradient direction. A simple stepper motor is envisioned to turn the gradient magnet ring. The advantages of a configuration consisting of homogeneous Halbach magnet and quadrupolar Halbach gradient are: a) only the Halbach gradient (which is a lot lighter) and not the whole magnet needs to be rotated b) the homogeneous Halbach magnet can be used for traditional spatial encoding schemes using gradient amplifiers.

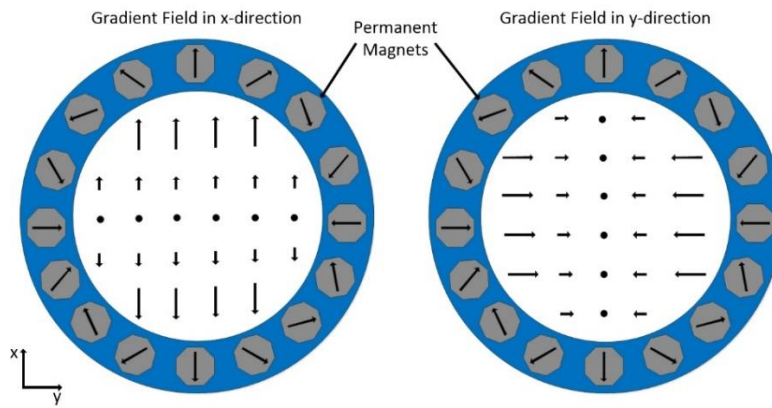


Figure 9: The two orthogonal gradient fields of a quadrupolar Halbach magnet ring.

The other parts of the COSI MR-System are relatively similar to a conventional MR scanner system. A schematic of the implemented system is shown in Figure 10. An RF coil is used to excite the nuclear spins in the sample and to detect the induced NMR signal. The RF coil is connected to the output of an RF power amplifier and to the input of a low noise preamplifier via a transmit-receive switch (Figure 10). The custom made RF power amplifier amplifies the RF-pulse and the low noise preamplifier reinforces the weak MR-signal to stabilize it for analog digital conversion. The spectrometer controls the timing of the sequences, produces the RF pulses, unblanks the RF power amplifier, digitizes the acquired MR-signal, steers the stepper motor to control the rotation of the gradient field and interfaces with the host-computer. In the following subchapters the implementation of those components is explained.

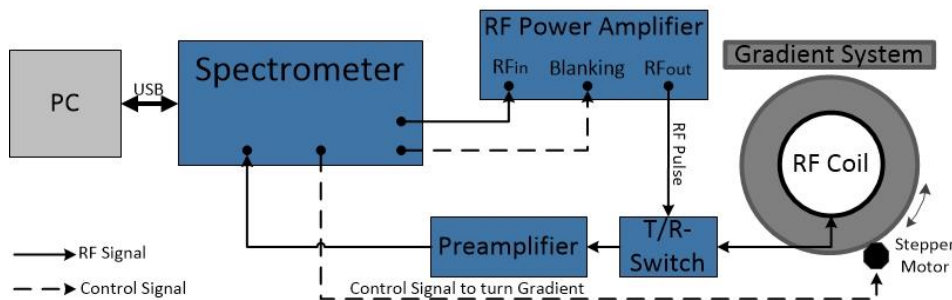


Figure 10: Schematic of the implemented COSI MR-system.

## 3.2 The Spectrometer

### 3.2.1 Spectrometer Hardware

In recent years, many advances and efforts have been made in research to develop, implement and improve customized NMR spectrometer hardware. One of the major goals was to meet the unique needs of special applications such as low field MRI by increasing configurability, portability and scalability and/or reducing costs [29-38]. In general, much of the research in this field benefits from concepts developed in the engineering sector of telecommunication. The basic idea is to transfer as many of the signal processing steps – such as modulation and filtering – from the analog to the digital domain. Accordingly, many systems have been developed around digital signal processors (DSPs) or field programmable gate arrays (FPGAs) which are used to execute pulse sequences and control external digital components [30-33] such as direct digital synthesizer (DDS) chips for RF pulse generation, digital down converter (DDC) to perform demodulation and quadrature modulation, analog digital converters (ADC) and digital analog converters (DAC) for signal sampling and analog signal generation respectively. The use of integrated circuit chips in combination with FPGAs and/or DSPs simplifies the design and greatly enhances flexibility as the digital components are programmable. Other designs [35-38] go even further by eliminating most of the external digital components (DDC and DDS) and implementing their functionality as modules within the FPGA. Thus, bringing the hardware efforts down to a minimum. Despite the advantages these approaches can offer in terms of flexibility and efficiency, replication by others is challenging for non-electronic experts due to the complexity of FPGA programming and the need to recreate the underlying hardware circuitboard. In contrast to that, Hasselwander et al. [39] recently demonstrated the use of a commercial available and ready to use software defined radio (SDR) as MR spectrometer. Therefore a software framework (gr-MRI) based on the open source software GNU Radio [40] was established to be used for the programming of MR imaging techniques. Since a SDR is equipped with complete analog frontends, it can directly interface with the RF- and gradient-amplifiers as well as the preamplifier and hence doesn't require additional hardware components.

The requirements for the COSY spectrometer are low cost, an operation frequency range from 3.4MHz to 12.7MHz ( $B_0=0.08\text{T}-0.3\text{T}$ ) and a compatibility with a custom made RF power amplifier. While in principal a FPGA based spectrometer fulfills all of those conditions, the design of an appropriate circuit board or the recreation of an existing design and the involved FPGA programming via a hardware description language are very time consuming and error-prone. With respect to the intended open source approach of the final system an individual hardware solution might have a dissuasive effect on possible imitators due to the same reasons. The utilization of a GNU Radio [40] compatible SDR in

combination with gr-MRI [39] or another open source framework enables hardware independent developments of new imaging techniques, a strategy that is in line with the collaborative approach of the open source imaging initiative [4]. Further advantages of SDRs are the integrated ADCs and DACs, the embedded USB- or Ethernet-interface as well as the comprised FPGA for basic filtering and signal down- and up-conversion. Moreover, GNU Radio compatible SDRs come with FPGA software images so that no programming via a hardware description language is required. For all those reasons a SDR was used as a spectrometer for the COSY MR-system.

The next section will introduce the reader to the basics of SDRs, motivate the choice of the SDR board and explain the structure of the implemented spectrometer.

### 3.2.2 Software Defined Radio (SDR) Spectrometer

#### Basics of SDR:

The basic idea behind a SDR is that one general-purpose hardware device can be used to realize many different communication or radio systems simply by exchanging the software that is controlling the device. Thereby, the term communication or radio system implies any system where analog signals are transmitted and/or received; in the case of a MR spectrometer this would be the generated RF pulse and the received MR signal. In order to achieve this kind of flexible architecture, a reconfigurable processor such as a FPGA forms the core part of the SDR hardware board. There, all the necessary digital signal processing tasks like DDC, DUC and filtering are performed. ADCs and DACs provide the interface to the analog world. Analog front end circuits on the receive side are used to extract a dedicated frequency band of interest and convert it to a baseband signal which is suitable for the ADC. In the transmit path analog front end circuits shift the baseband signals produced by the DACs to the designated carrier frequency. This approach allows to accurately detect and digitize RF signals and reliably transform digital samples into an analog signal over a wide range of frequencies [41, 42]. The following paragraph will give an overview on existing SDRs and motivate the choice of the SDR finally used for the COSY spectrometer.

#### Choice of SDR board:

There exist many different, off-the-shelf SDR models offered by several manufacturers and companies. They differ from one another in terms of their operation frequency range, the number of provided RF channels, their maximum bandwidth, the capabilities of their integrated ADCs and DACs and the supported software tools that allow access and programming. Their price range from a few hundred to a few thousand euros. The requirements to the SDR for the COSY spectrometer are coverage of the



frequency range from 3.4-12.7MHz, at least three<sup>1</sup> analog RF transmit (TX) channels and two<sup>2</sup> analog RF receive (RX) channels, GNU Radio compatibility and low cost (<2000€). Several different SDRs were taken into consideration. The HackRF One is a hardware open source SDR produced by Great Scott Gadgets [43]. It covers a frequency range from 1 MHz to 6 MHz, is GNU Radio compatible and features ADC with a sample rate of 20 million samples per second and a resolution of 8 bit. Even though the complete open source approach is appealing, with only one half-duplex RF TX/RX channel the HackRF One is not capable of simultaneously transmitting and/or receiving multiple signals. However, this is a key requirement for the intended spectrometer design. For example the RF pulse and the unblanking pulse for the RF power amplifier need to be generated at the same time. Another option is the Red Pitaya [44], a multi-purpose-instrumentation board which runs its own operation system on an onboard ARM processor. It features two fully independent RX and two fully independent TX channels which cover a frequency range from DC to 50 MHz and both, the ADCs and the DACs have a sampling rate of 125 MS/s and a resolution of 14 bits. Hence, the Red Pitaya fulfills all the technical requirements. Unfortunately it does not support GNU Radio and hence is not gr-MRI compatible. Beside those two options there exist many SDRs with an operation frequency range starting from a couple of MHz to a few GHz. The USRP B200/B210 from Ettus Research [45] for example fulfills all requirements but covers a frequency range from 70MHz-6GHz. Consequently, all SDRs with a higher operation frequency range are not applicable from the start. The remaining SDRs which are eligible from a technical point of view – like the Crimson TNG from the company Per Vices Corporation [46] (price 6000€) – are too expensive to be considered for an affordable low cost MR system.

Finally, the USRP1 from Ettus Research [47] was chosen as most suitable SDR for the COSY spectrometer. The USRP1 – shown in Figure 11 – fulfills all the necessary requirements and is with a price below 1000€ still affordable. It has an operational frequency range from DC to 6 GHz, provides up to 4 TX and 4 RX channels and the integrated dual ADCs and DACs provide sampling-rates of 64 MS/s and 128 MS/s with a resolution of 12 and 14 bits respectively. Hence, the performance capabilities of the ADCs and DACs lie within the range of what commercial MR spectrometers offer. Furthermore, the host-sampling rate between USRP1 and PC – which defines the maximum baseband sampling rate of the system – is with 8 MS/s high enough to allow sufficient readout bandwidth for MR experiments. Consequently the USRP1 is the best choice for the intended COSY spectrometer.

The following section will introduce the reader to the general structure of a USRP family based SDR system since the chosen USRP1 SDR belongs to that series.

---

<sup>1</sup> Three analog TX channels for generation of RF pulse, readout window control signal and unblanking signal for RF power amplifier.

<sup>2</sup> Two analog RX channels for reception of NMR signal and fed-back readout window control signal.

### The USRP Family by Ettus Research:

In general, all SDR systems that are based on the USRP family consist of three main hardware components: a common **personal computer** (PC), a **USRP motherboard** and one or more **RF daughterboards** which are connected to the motherboard. Thereby, the RF daughterboards serve as analog frontends to convert the analog signals from the frequency bandwidth of interest to the baseband and vice versa. They contain quadrature up- and down-converters, amplifiers with gain control, filters and local oscillators. The motherboard is the bridge between the analog world and the digital domain of the personal computer. They are connected via an asynchronous interface such as Ethernet or USB. The computer runs the user's SDR application which defines the functionality of the whole system and controls the motherboard using the USRP Hardware Driver (UHD) library. The FPGA on the motherboard is responsible for the required timing and control tasks and does the necessary signal processing. The FPGA also passes quadrature baseband digital samples – coming from the host computer – towards the ADCs, and similarly sends the digital samples coming from the DACs back to the computer [41].



*Figure 11: USRP1 motherboard from Ettus Research equipped with one receive LFRX daughterboard and two transmit LFTX daughterboards.*

### Implementation of the COSI Spectrometer:

The implemented COSI spectrometer utilizes the gr-MRI software package presented in [39]. This software package is programmed for the open source software GNU Radio [40]. GNU Radio is a visual programming language similar to LabVIEW or Simulink where the user creates a so called GNU Radio flowgraph by connecting different blocks via wires. Each block implements a certain function – for example multiplying two complex numbers – and by combining multiple blocks a whole system can be realized. Thereby, the data samples flow along the wire-connections from the left side to the right side of the flowgraph. The sample rate  $f_A$  defines at which rate the flowgraph is executed. Special blocks, so called sink- and source-blocks are used to establish a connection between the flowgraph, running on the host computer and the USRP1 motherboard in order to control the board and to transmit and receive data. Therefore, GNU Radio uses the interface provided by the UHD library. The implemented

flowgraph is then translated into python code and defines the whole functionality of the system. It runs as SDR application on the host computer. The software package gr-MRI [39] provides two new customized blocks to be used in a GNU Radio flowgraph namely the *gated\_vector\_source* and the *gated\_vector\_sink*. Those blocks enable the realization of standard MRI sequences in a GNU Radio flowgraph. The first block allows to store samples of a user defined excitation pulse in a vector which is outputted whenever the input to the block is high. Otherwise zeros are played out. The second block is able to record the NMR signal in a certain acquisition window and stores it in a vector whenever the input to the block is high. Together with a python script which is used to start the flowgraph and adapt MR relevant parameters such as echo time (TE), inversion time (TI), repetition time (TR), Larmor frequency, RF pulse length and amplitude, readout length and bandwidth, the USRP1 can be used as an MR spectrometer [39]. In total, Hasselwander et al. [39] have used two USRP1 motherboards: One to create the RF-pulse and the associated blanking signal for the RF-power amplifier and to receive the NMR signal; and a second board to generate the three gradient pulses required in a traditional MRI system. They have successfully used this spectrometer to control a standard MRI desktop scanner and acquired images with a spin-echo, a gradient-echo and an inversion recovery sequence.

This work has been used as basis to the implemented SDR spectrometer and was adapted and extended according to the requirements of the COSY MR-system. In contrast to Hasselwander et al. [39] only one USRP1 motherboard is required since the COSY MR-system does not have a conventional gradient system which makes the second board redundant. Instead, the rotational gradient system is controlled via the general purpose input output (GPIO) pins available on the daughterboards. The schematic in Figure 12 gives an overview on the structure of the implemented SDR spectrometer. The following descriptive text refers to this schematic. The GNU Radio flowgraph defines the functionality of the USRP1 board (the composition of the flowgraph will be explained later). It runs as a process on a PC and continuously transmits and receives digital baseband samples via USB to and from the USRP1 board. The flowgraph itself is started and controlled by a python script which is executed in an iPython console [48]. This python script provides functions to change sequence parameters – such as repetition time (TR), RF-pulse length and amplitude, readout delay and acquisition window etc. –, to initiate a sequence and to store the acquired data to a file. The functions can be invoked from the iPython console in which the script was started. To initiate a sequence, the according function first stops the flowgraph, then deletes all the data stored in the flowgraph that has been previously acquired and finally restarts the flowgraph. After the specified scan time has elapsed, the flowgraph is stopped again and the acquired data is loaded from the flowgraph and stored as complex numbers in a local variable on the personal computer. The scan time is determined by the repetition time and the number of averages.

The USRP1 board was equipped with two LFTX transmit daughterboards [49] (LFTX A and B in Figure 12) and one LFRX receive daughter board [50] (LFRX A in Figure 12). They both cover a sufficient frequency range from DC to 30 MHz ( $B_0=0-0.7T$ ) and provide two analog RF channels marked as A and B. The LFTX A board is used to generate the RF pulse and a control signal to indicate the readout window. Those two signals are combined as real and imaginary part to a complex signal, are modulated to the Larmor frequency and are then outputted on both channels (identical signals on channel A and B) of the LFTX A board. The signal on channel A is sent to the RFPA. Thereby, the fact that along with the RF pulse also the control signal for the readout window is send to the RFPA is not problematic since unblanking of the RFPA is only applied during the RF pulse. Thus, just the RF pulse itself will be amplified. The signal on channel B of the LFTX A board is fed back to channel B on the receive board LFRX A. This back-feeding-mechanism serves two purposes. First, to control data acquisition and second, to remove spectrometer phase drifts. The details of this mechanism will be explained later together with the structure of the flowgraph. On the second transmit daughterboard (LFTX B) the control signal to unblank the RFPA is outputted on channel A as a DC signal with an amplitude of 1V. Further, the GPIO pins on the LFTX B board are used to generate the required pulses to control a stepper motor which allows turning the gradient field. One positive pulse edge at the control input to the motor-driver will cause the stepper motor to turn by one step. Accordingly, two consecutively edges will cause the motor to turn two steps and so forth. The rotation step length of the motor can be specified in the settings of the motor-driver. The pulses are generated from the python script in between two projections of an MRI scan using functions of the USRP Hardware Driver (UHD) library to set and reset individual GPIO pins on the LFTX B daughterboard.

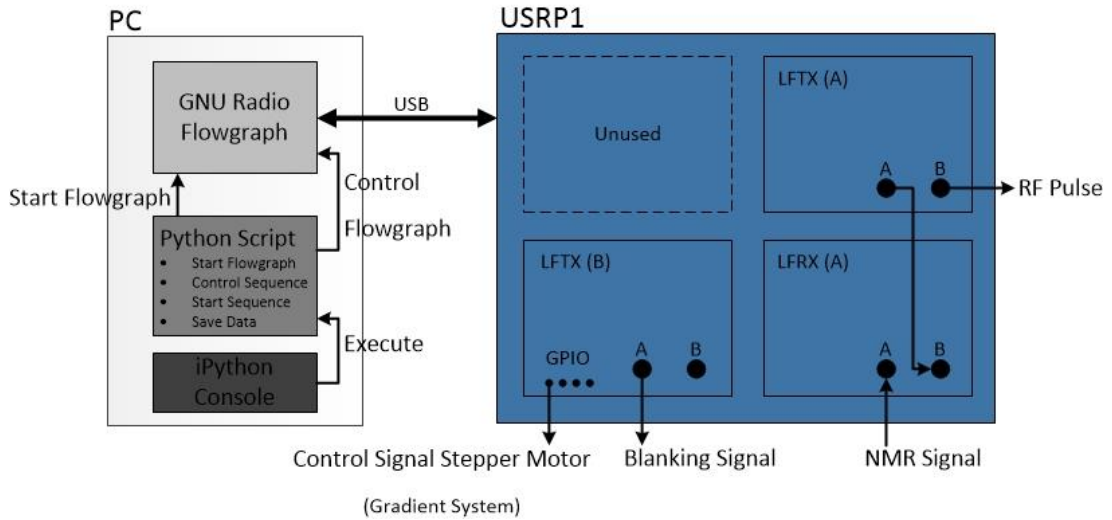


Figure 12: Schematic of the implemented SDR spectrometer.

Figure 13 illustrates the composition of the implemented GNU Radio flowgraph. The upper half shows the transmit section and the lower half the receive section. Once started, the flowgraph runs continuously. Its execution rate is defined by the sample-rate  $f_A$ . The transmit section is triggered by

the positive edge of a square wave with the frequency  $f=1/TR$  which is produced by a signal source block. Changing the frequency of the square wave enables the user to control the repetition time of the sequence. The pulse shape of the excitation pulse is stored as a complex vector in the upper gated vector source block. It is played whenever the block detects a positive trigger signal. Similarly, the readout signal is stored and played by the second gated vector source block with the difference that the trigger signal is delayed by the readout delay and the length of the excitation pulse. Both pulses are added and send to the USRP1 sink block. The settings in the USRP1 block define to which daughterboard the signal is transmitted and whether it is outputted at only one channel (A or B) or as real and imaginary part on both channels. Further the carrier frequency and an amplification factor are set. The signal data and the control information are then transmitted via USB to the motherboard and from there to the according transmit daughterboard. In the implemented flowgraph the signal is send to the LFTX A daughterboard and outputted at the Larmor frequency of the sequence as real and imaginary part on both channels A and B. On the second daughterboard (LFTX B) the unblanking pulse for the RFPA is outputted at a carrier frequency of zero hertz (DC signal) on the channel A. It is generated by applying a moving average filter on the RF excitation pulse with a user defined factor to prolong its length as compared to the RF pulse length.

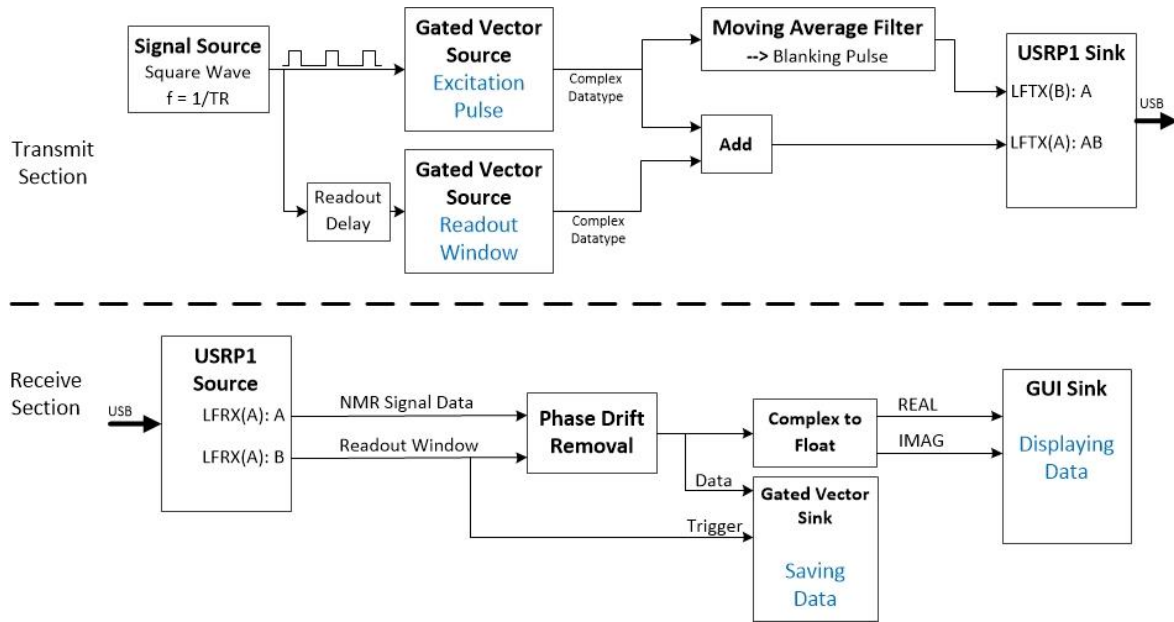


Figure 13: Schematic of the implemented GNU Radio Flowgraph for the MR spectrometer.

In the receive section the acquired data is entering the flowgraph via the USRP1 source block. There it is defined from which daughterboard the signal is coming and the carrier frequency of the signal. Further, an amplification factor (max 20dB) can be set which will enhance the signal prior to analog digital conversion. In the implemented flowgraph the upper data stream represents the NMR signal data. It is connected to channel A on the daughterboard LFRX A. The center frequency of the channel is set to the Larmor frequency and the amplification factor to 15dB. The lower data stream is linked to

channel B on the LFRX A daughterboard on which the readout window signal is received directly from the LFTX A board. The center frequency is also set to the Larmor frequency and the signal is amplified by 10 dB. Before saving and displaying the received data the spectrometer phase drift is removed. This is done by multiplying the NMR signal with the complex conjugate of the normalized readout window signal. This is possible because the excitation pulse and the readout window pulse originate from the same daughterboard and hence experience the same phase drift [39]. The readout window pulse is then used to trigger the gated vector sink block to save the NMR signal in a complex data vector. Additionally, the data is displayed in a time sink GUI.

### 3.3 The RF Power Amplifier

The purpose of an RF power amplifier (RFPA) in a MRI system is to amplify the RF excitation pulse produced by the spectrometer before it is sent to the transmit coil. This is necessary in order to reach high  $B_1^+$ -field amplitudes which allows shorter excitation pulses while maintaining the same flip angle. Requirements to a RFPA in MRI are high linearity and phase and amplitude stability over the entire pulse length [51]. Further, blanking of the RFPA during the rest of the sequence is essential to avoid noise-leakage from the RFPA output into the NMR signal while data acquisition. Typically, RFPAs in MRI systems provide an output power level of several kilo watts. For the COSY MR-system, a RFPA with a maximum output level of 1kW is designated. Unfortunately, there are only few commercial RFPAs in that low frequency range available that offer such a high output power. Those available, like the HF 1000 RF PALLET (1kW, 1.5-35MHz, 480€ [52]) and the HF 1000 BX (1kW, 1.8-50MHz, 500€ [53]) do not provide the possibility for blanking/unblanking, are not open source and require an input signal with a power level of several watts (5-10W) which is not possible to directly generate with the intended spectrometer.

In collaboration with the PTB Berlin an RFPA module has been designed and constructed. A schematic of the RFPA is shown in Figure 14. It consists of a driver stage, an amplification stage, a filter, a blanking circuit and a cooling circuit. As a driver, a two stage linear amplifier design [54] with 33-34dB gain and an output power of 5W is used in order to cover a wide range of input voltages that allow an amplification to the intended 1kW of the amplification stage. The driver stage is powered by a 12V DC supply voltage. The amplification stage [55] is based upon a power LDMOS transistor (BLF188XR, 1400W, NXP, Eindhoven, Netherlands) which is flow-soldered to a copper heat spreader block. The heat spreader itself is mounted onto a heat sink which is attached to a fan for optimal cooling of the transistor. The final amplification requires a 50V DC power supply. The filter at the output is a 6-segment, selectable low pass filter which covers a frequency range from 1.8MHz to 54MHz [56] and is designed for a power level of up to 1.5kW. It is necessary in order to suppress unwanted harmonics.

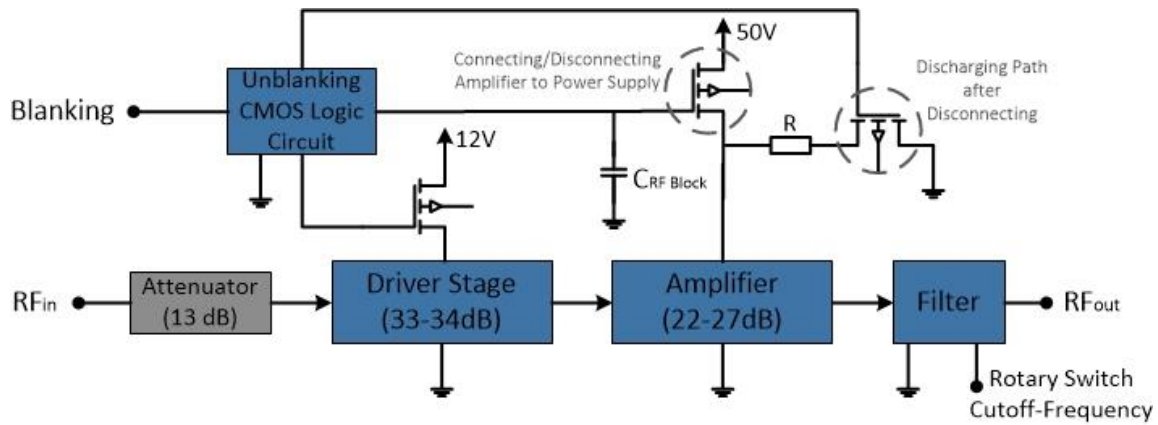


Figure 14: Schematic of the implemented RFPA with 1kW output peak power and a frequency range from 1.8-54MHz.

The 13dB attenuator at the input is needed to adjust the RFPA to the output range of the SDR spectrometer (+/-500mV). Unblanking of the RFPA is done at a high TTL voltage level. To blank and unblank the RFPA the connection of both amplification stages to the power supply is switched off and on respectively via a dedicated CMOS transistor logic circuit. For the final amplification stage it is further necessary to discharge several capacitors ( $C_{sum} \sim 200\mu F$ ) that are fitted between the supply voltage and ground to prevent oscillations on the power supply voltage. Discharging of the capacitors is done via a CMOS transistor and a resistor. The implemented RFPA covers a frequency range from 1.8MHz to 54MHz, provides an output peak power of 1kW and falls in the AB class of RFPA's. AB class amplifiers combine the good linearity characteristics of class A amplifiers with the more efficient power performance of class B amplifiers. Electronic circuits of the driver and amplification stage are available from ([http://www.box73.de/product\\_info.php?products\\_id=1899&XTCsid=86316710323ff4cb4d6e8857b9a31277](http://www.box73.de/product_info.php?products_id=1899&XTCsid=86316710323ff4cb4d6e8857b9a31277)) and (<http://www.w6pql.com/index.htm>) respectively.

Since the design of the implemented spectrometer necessarily generates the RF pulse and the readout control signal on the same channel, the control signal will also appear at the RFPA input. Therefore it is crucial that the integrated HF blocking capacitors are discharged very rapidly. Otherwise the remaining voltage over the capacitors will lead to an amplification of the readout control signal which would disturb signal acquisition. Unfortunately, the intended solution to discharge the capacitors via a  $0.2\Omega$  resistor and a CMOS transistor was not sufficient. Figure 15 shows the beginning and the end of the RFPA unblanking pulse. Thereby, the green curve represents the unblanking pulse as it appears at the unblanking input of the RFPA. The blue curve shows the course of the 50V supply voltage as it is connected and disconnected to the final amplification stage. As it can be seen from the graph, discharging the capacitors requires over  $100\mu s$ . This performance is not adequate and would introduce a mandatory minimum delay between the RF pulse and the signal acquisition until the RFPA is successfully blanked. Similarly, the capacitors delay the turn on of the supply voltage.

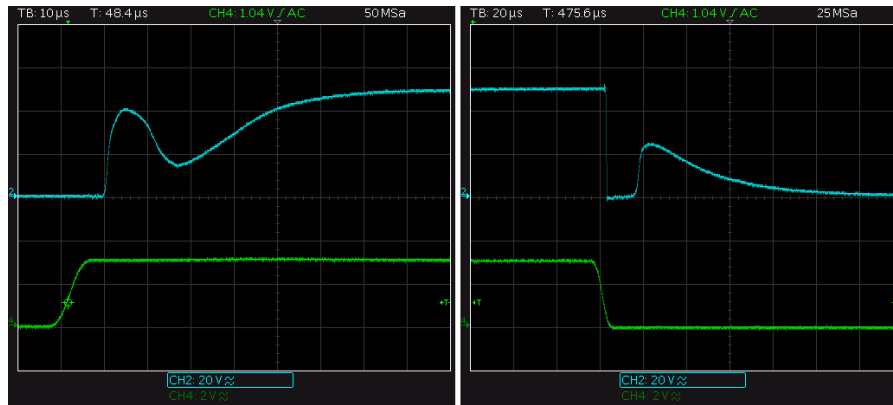


Figure 15: The graph shows the beginning and the end of unblanking pulse of the RFA (green) and the corresponding course of the 50V power supply voltage of the final amplification stage (blue) prior to removing the RF blocking capacitors.

To solve this problem, the RF blocking capacitors were removed from inside the amplifier and inserted after the transistor that performs the clamping of the supply voltage. In this configuration the relatively large capacitors do not have to be charged and discharged anymore. The graph in Figure 16 reveals the improvement accomplished by this modification. It is clearly visible, that the 100 $\mu$ s long exponential decay of the supply voltage has disappeared and the clamping now happens with a very sharp edge. The small peak that is still visible results from the discharging of the remaining HF blocking capacitors ( $\sim 2\mu$ F) in amplifier circuit. Hence, the systems performance is not limited anymore. Also the switching on period of the unblanking is improved, however not as much as expected. As a solution to this, the unblanking of the RFA by the spectrometer will be performed 150 $\mu$ s prior to the RF pulse application so that the supply voltage can stabilize during that time.

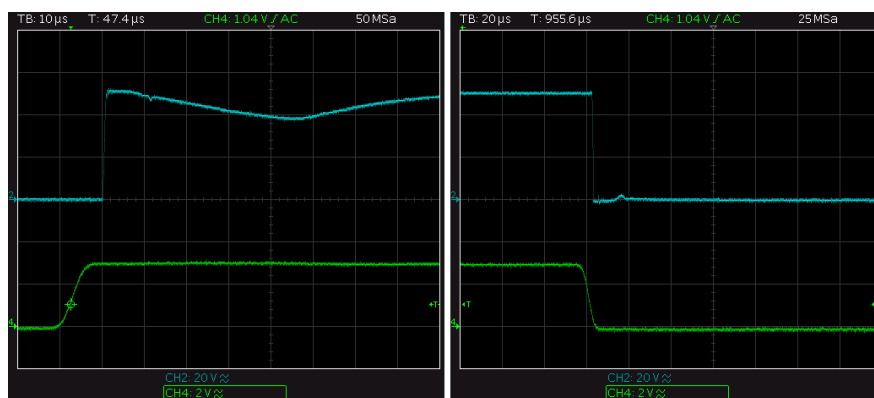


Figure 16: The graph shows the beginning and the end of unblanking pulse of the RFA (green) and the corresponding course of the 50V power supply voltage of the final amplification stage (blue) after the RF blocking capacitors were removed and put behind the switching transistor.

In order to reach the necessary TTL voltage level for the unblanking of the RFA, a voltage level converter is used at the output of the spectrometer since the SDR is only capable of producing signals in the range of  $\pm 1$ V. The level converter raises the amplitude of the rectangular unblanking pulse from +1V to +3V. Therefore a simple non-inverting amplifier circuit around an operational amplifier (TLC272, Texas Instruments, Dallas, USA) is used. Figure 17 a) shows the structure of the circuit. It is supplied



with a 6V DC voltage which is provided by a common power supply unit. The ratio of the resistance  $R_1=10k\Omega$  to the resistance  $R_2=4.7k\Omega$  sets the amplification factor of the circuit to  $G = 1 + R_1/R_2 \approx 3$ .

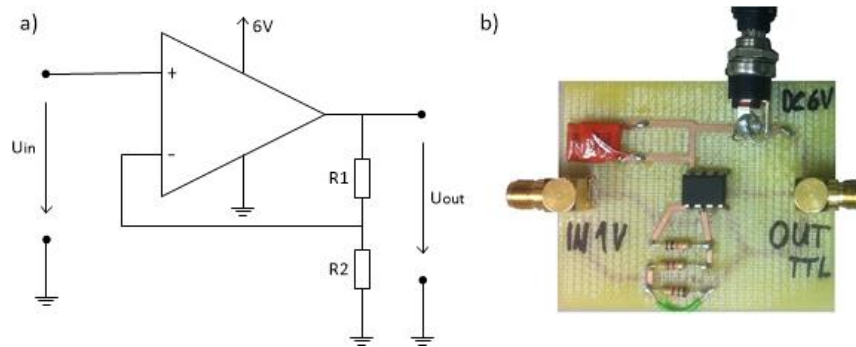


Figure 17: a) Circuit diagram of the implemented level converter to convert the amplitude of the RFPA unblanking pulse from 1V – produced by the spectrometer – to TTL level. b) Picture of the Level Converter.

### 3.4 The Transmit/Receive-Switch

A transmit/receive-switch (T/R-switch) is an electronic device in a radio system that allows to alternatingly connect a common RF antenna either to the receive-path or to the transmit-path of a system. In a MRI system it is used to connect the RF coil to the output of the RFPA and to the input of the preamplifier. In general, there exist active and passive T/R-switches, with the active devices requiring an external control signal for switching. Requirements to a T/R-switch in MRI are high isolation between the TX port and the RX port in order to avoid damage of the preamplifier by the high power RF pulse, low insertion loss on the receive path to keep attenuation of the acquired NMR signal as low as possible and endurance of high input power levels in the range of 1-2kW. For the COSY MR-scanner the T/R-switch must be capable of dealing with a maximum peak power of 1kW which is the output power of the constructed RFPA. Furthermore, the isolation between TX port and RX port must be greater than 38 dB since the maximum input power to the utilized preamplifier is 100mW (20dBm). Finally, and most important the working frequency range of the T/R-switch must include the designated center frequency (3.5-4.5MHz) of the prototype magnet. One of the few commercial products available that feature these high power requirements is the passive transcoupler provided by NMR Service GmbH (Erfurt, Germany, [57]). This T/R-switch – shown in Figure 18 – accepts a maximum input power of 1.3kW (50ms pulse), offers 47dB isolation between the TX and the preamplifier port, has a receive attenuation of 0.3dB and covers a frequency range from 3-5MHz. It was purchased as a firm basis for the COSY MR-system and might be replaced in a later stage of the project by a customized open source solution.

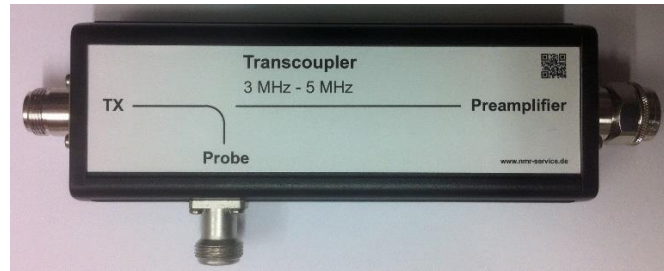


Figure 18: Passive T/R-switch produced by the company NMR Service GmbH (Erfurt, Germany).

### 3.5 The NMR Signal Preamplifier

The preamplifier is after the receive coil the second most important component concerning the sensitivity of the whole MRI scanner. While the properties of the RF coil determine the magnitude and quality of the received NMR signal, the preamplifier is responsible for amplifying the signal and at the same time adding as little noise as possible. Consequently, low noise amplifiers (LNAs) are utilized. To avoid losses in the connecting cables the preamplifier should be placed as close as possible to the coil. Amplification prior to analog digital conversion is necessary to strengthen the signal and to fully exploit the dynamic range of the ADC [58].

Important parameters to describe the characteristics of a preamplifier are the amplification factor  $G$  and the noise figure N.F. Both parameters are commonly indicated in dB. The amplification factor  $G$  is defined as the ratio between the signal level  $S_{out}$  at the output to the signal level  $S_{in}$  at the input of the amplifier and is therefore a measure for the signal enhancement. The noise figure is defined as the quotient of the signal to noise ratio at the input of the amplifier to the signal to noise ratio at its output. Hence, it specifies how much noise is added by the amplifier to the amplified signal. In MRI systems usually a cascade of multiple amplification stages is used. Thereby, the overall N.F. is essentially influenced by the first amplification stage. Consequently, the preamplifier should provide a relative high gain and a N.F. as low as possible. Good values for the NF are as low as 1dB [59].

For the COSY MR-system a preamplifier working in the lower MHz frequency range is needed. Unfortunately, this requirement excludes many commercial available LNAs specifically tailored for MRI applications since the working frequency in traditional MR technology starts from around 40MHz. Nevertheless, there exist commercial products provided by companies such as NMR Service (Erfurt, Germany), Teseq GmbH (Reinach, Switzerland) or HD Communications Corp. (Holbrook, USA). However, the price of those devices lies between 500€ and 1000€ and is thus too high for a first prototype system. Instead, a cheap (20€) LNA design from the radio community is used (LNA4HF) [60]. A photograph of the device is shown in Figure 19. It covers a frequency range from 150 kHz to 30 MHz, provides 18-20 dB of gain and a N.F. of 1-2dB and requires a supply voltage between 6 and 9V which can easily be obtained from the 6V power supply of the SDR board. These characteristics are expected

to be sufficient for a proof of principle. The performance of the LNA4HF in its current configuration is limited by the integrated Monolithic Microwave Integrated Circuit (MMIC). Substituting the MMIC (MAR-6SM+, Mini-Circuits, Brooklyn, USA) with another chip that has for example a lower N.F. or higher gain could further improve the current design. Another option is to replace the LNA4HF by a more sophisticated LNA in a later stage of the project when the exact center frequency of the constructed prototype magnet is known. This allows the utilization of a small bandwidth LNA which significantly reduces noise. The company Advanced Receiver Research (Burlington, USA) for example offers LNAs with a N.F. of 1.1 dB and gain of 26 dB with a bandwidth of 200-300 kHz.

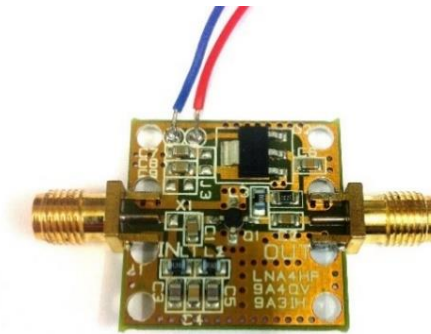


*Figure 19: Photograph of the LNA4HF which is used as preamplifier. It covers a frequency range of 150 kHz – 30 MHz and provides a gain of 18-20 dB and a N.F. of 1-2dB.*

## 3.6 The RF Coil

The RF coil represents the interface between the sample and the MRI scanner. As such, it is a crucial part of the system and should be planned and designed carefully since it defines the transmit- and receive-capabilities of the whole system. The next sections will introduce the reader briefly to the basics of RF coil design, discuss the RF coil design, explain the electromagnetic field simulations which were performed to optimize the RF coil geometry and describe the  $B_1^+$  field validation measurements that were performed.

### 3.6.1 Basics

#### RLC Resonance Circuit:

An RF coil is basically an electrical resonance circuit tuned to the Larmor frequency of the designated MR experiment. In a simplified schematic it consists of an inductance  $L$ , a capacitor  $C$  and a resistor  $R$  in a serial or parallel configuration (RLC circuit). Resonance occurs when the imaginary parts of the inductance and the capacitor cancel each other out. In this case the input impedance to the RLC circuit becomes purely real. The resistance  $R$  includes the different loss mechanisms that are present in an RF coil. Neglecting the loss mechanisms, the resonance frequency  $\omega_0$  is given by the following equation [61]:

$$\omega_0 = \sqrt{\frac{1}{LC}} \quad (5)$$

In the case of resonance, the magnetic and the electric energy stored in the circuit are equal and oscillate between the inductor and the capacitor. As equation (5) demonstrates, the resonance frequency  $\omega_0$  is solely depended on the values of L and C [58, 62].

#### Loss Mechanisms in a RF Coil:

The loss mechanisms present in a RF coil lead to a potential difference in the inductive loop which is added to the detected NMR signal. The effective noise signal magnitude  $\sigma_{\text{Noise}}$  can be expressed as:

$$\sigma_{\text{Noise}} = \sqrt{4 * R_{\text{eff}} * k_B * T * \Delta f} \quad (6),$$

where  $k_b$  is the Boltzmann constant, T the temperature of the RF coil and  $\Delta f$  the bandwidth of the detected NMR signal. The losses are summarized in the effective loss resistance  $R_{\text{eff}}$ . In total, three different loss mechanisms contribute to  $R_{\text{eff}}$ : resistive losses  $R_\Omega$ , electric losses  $R_E$  and magnetic losses  $R_M$ . They are added to form the effective loss resistance:

$$R_{\text{eff}} = R_\Omega + R_E + R_M \quad (7)$$

The resistance  $R_\Omega$  involves all “ohmic” values of the electrical conductors, such as wires, used in the resonance circuit. The resistance is thereby larger than the direct current resistance due to the skin effect which reduces the current density inside of the conductor and forces most of the current to flow in proximity to the conductor surface. The electric losses  $R_E$  are caused by high potential differences between ground and some circuit parts which lead to electric fields passing through the conductive sample. These electric fields induce currents in the sample and thus contribute to electric losses. Finally, the magnetic losses  $R_M$  are caused by the leakage due to the induced eddy currents in the conductive sample during the transmit phase [58, 62].

#### Tuning-Matching Circuit:

The coupling of the RF coil with its surrounding environment – especially with the sample – changes the resonance frequency and the input impedance  $Z_{\text{in}}$  of the RF coil. Therefore, a method is required which allows to individually tune and match the RF coil to different sample loadings. This can be achieved by a so called tuning-matching circuit which is integrated between the input terminal of the RF coil and the resonance circuit itself. Matching of the RF coil to 50  $\Omega$  – which is the standard in MRI systems – is necessary in order to avoid reflection losses at the input of the coil. One possible realization of a tuning-matching circuit is depicted in Figure 20. It consists of two variable capacitors

$C_{\text{tune}}$  and  $C_{\text{match}}$  which are placed in parallel and series at the input terminal of the RF coil respectively. With this setup the real and imaginary part of the coils impedance can be changed to tune and match it [58].

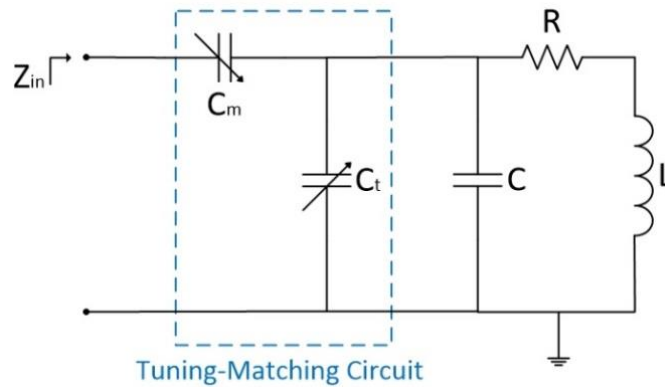


Figure 20: Series RLC resonance circuit with capacitive tuning-matching circuit.

#### RF Coil Characterization with a Network Analyzer:

Since a RF coil is an LC resonator it either reflects or absorbs electromagnetic waves that are transmitted to the coil. This ability is utilized to investigate and characterize the developed RF coil with a network analyzer. A network analyzer is an electronic measurement device which continuously generates sinusoidal signals with temporally increasing frequency. These signals are transmitted to the RF coil. At the same time, the network analyzer measures the signal levels reflected from the RF coil and plots them over the frequency range of the input signal. At the RF coils resonance frequency most of the energy transmitted to the RF coil is absorbed and thus only little is reflected, whereas at the other frequencies most of the signal is reflected and almost nothing is absorbed. Hence, the resonance frequency is clearly recognizable from a distinct negative peak. This measurement method is referred to as  $s_{11}$  reflection based upon the 4-port network theory which can be used to describe any electronic unit by its frequency-dependent complex s-parameters. It enables the precise determination of the resonance frequency, the quality of the matching and the quality factor (Q-factor) of the RF coil [61, 62].

### 3.6.2 The RF Coil Design

The COSI MR-System features – unlike clinical MR scanners – a static magnetic field  $B_0$  perpendicular to the scanners bore axis. These characteristics influence the choice of the RF coil used. While conventional scanners typically use a birdcage RF coil design, in a Halbach magnet based system a simple solenoid RF coil can be implemented in order to generate the necessary RF excitation pulse and detect the MR signal [58]. Such solenoid RF coil designs have already been used in other MR systems with vertical  $B_0$  fields at field strengths below 0.3T [17, 63] and proven to provide images of good

quality. A solenoid transmit and receive RF coil features a very homogeneous  $B_1^+$  field during excitation and offers the highest SNR capabilities among volume RF coils during signal reception [58]. Furthermore, it is relatively easy to design and construct compared to a birdcage RF coil design. For those reasons a solenoid RF coil was developed and constructed to work as a transmit/receive volume RF coil in the COSI MR system.

### 3.6.3 Electromagnetic Field Simulations

Prior to building the intended solenoid RF coil, the electromagnetic field distribution inside of the solenoid was simulated for different helical structures of the RF coil (Simulation Software: CST MWS 2012, Darmstadt, Germany). The main goal of the simulations was to reach a homogeneous  $B_1^+$ -field distribution inside of a spherical sample with 70mm diameter representing muscular tissue (epsilon: 429, electrical conductivity: 0.58S/m, density: 1090kg/m<sup>3</sup>). Therefore, the maximum inhomogeneity within the sample was calculated as maximum relative difference from the  $B_1^+$  value in the RF coil center along the x-, y- and z-direction. The spherical sample was chosen to model a typical loading scenario of the RF coil. For the optimization process the number of turns and the length of the RF coil were treated as variables, whereas the inner coil diameter and the cross section of the electrical conductor were kept fixed. The inner coil diameter was set to 96mm so that the RF coil fits into the magnets bore (130mm inner diameter) and that a human hand can still be placed inside. As electrical conductor a copper wire (material properties: copper annealed, electrical conductivity: 5.8e7S/m, density: 8930kg/m<sup>3</sup>) with 0.85mm diameter was chosen which is in line with a similar design presented in [17]. The resulting 3D model of the solenoid RF coil and the sample is shown in Figure 21. The simulations were conducted for a resonance frequency of 3.63MHz which is the intended center frequency of the first prototype Halbach magnet. The mesh step size was set to 1mm with 232x241x201 mesh-cells in x-, y-, and z-direction respectively which results in 11.088.000 mesh-cells in total.

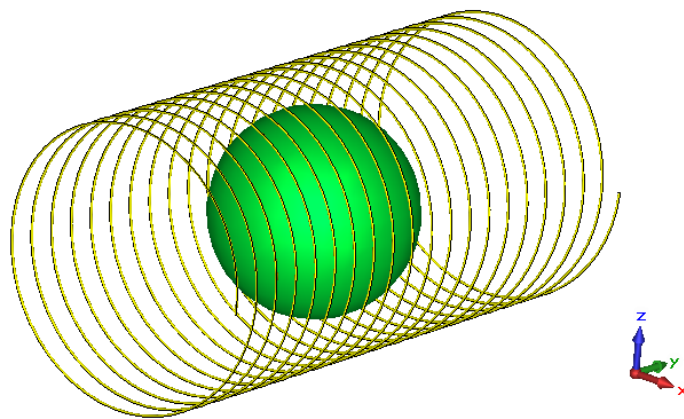


Figure 21: CST simulation model of solenoid RF coil (yellow) and spherical sample (green).

### 3.6.4 $B_1^+$ Field Validation Measurements

In order to measure the  $B_1^+$  field generated by the constructed solenoid RF coil, multiple  $s_{12}$  measurements between the solenoid RF coil (port 2) and a 10 mm diameter pickup loop (port 1) were acquired with a network analyzer (Rohde & Schwarz, München, Germany). Therefore, the pickup loop was positioned at one end of the solenoid coil and moved in steps of 10 mm along a straight line from one side of the opening to the other. Figure 22 shows a photograph of the measurement setup indicating the measurement path. At each position, an  $s_{12}$  measurement (center frequency 3.63MHz and frequency span 1MHz) was acquired. Relating the measured signal levels to appropriate calibration data of the pickup loop in a known B field allows the calculation of the  $B_1^+$  amplitude at each measurement position.

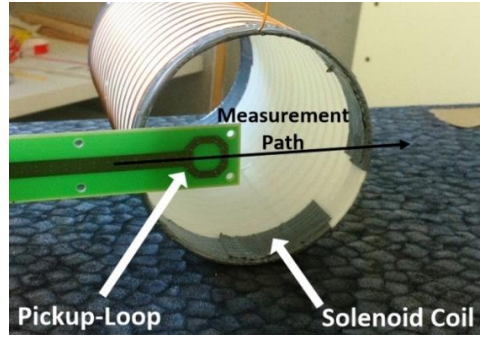


Figure 22: Photograph of the  $B_1^+$  field measurement setup for the constructed solenoid coil with a pickup loop positioned along the measurement path.

The pickup loop calibration was done in a so called Transverse ElectroMagnetic (TEM) cell which is providing a defined environment for electromagnetic measurements [64]. The TEM cell used for the calibration – shown in Figure 23 on the left side – is an open double stripline design with two identical electro-magnetic compartments and SMA connectors at the in- and output of the cell. The geometry of the cell is chosen to meet the typical wave resistance of  $50\Omega$  to avoid signal reflections. For a given RF input signal, this setup allows the calculation of the emerging electrical field  $E$  between the inner and outer conductor of the TEM cell with the following equation (given that the output of the TEM cell is terminated with a  $50\Omega$  wave resistance to avoid signal reflections):

$$E = \frac{U}{d} \quad (8),$$

where  $U$  is the voltage of the input signal and  $d$  the distance between the inner and outer conductor of the TEM cell (here 0.03m). The electrical field  $E$  is linked to the magnetic flux density  $B$  via the equation:

$$E = B * c_0 \quad (9),$$

with  $c_0$  being the velocity of light. These properties of the TEM cell allow the calculation of the B field magnitude inside the TEM cell for a given RF input signal.



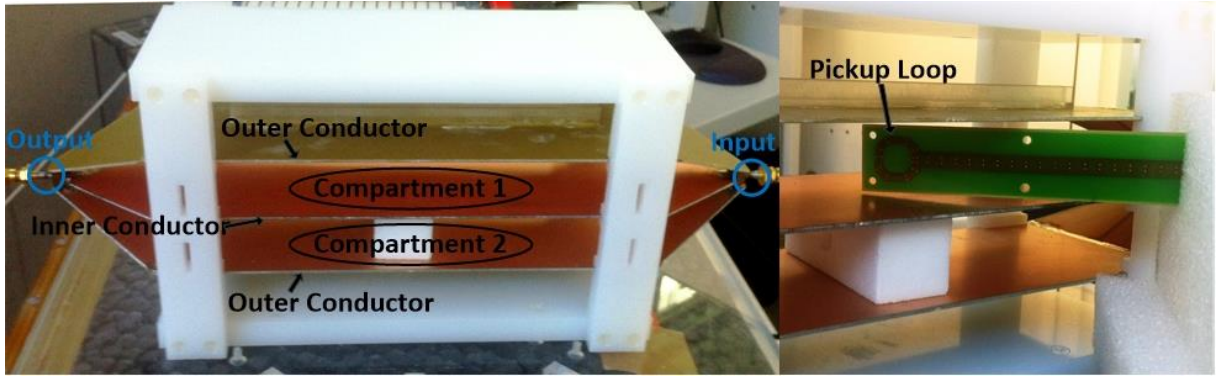


Figure 23: Left side: Transverse ElectroMagnetic (TEM) Cell used for the calibration of the pickup loop.  
Right side: Pickup loop inside of TEM cell for calibration.

This can be utilized to calibrate the pickup loop by an  $s_{21}$  measurement. Therefore, the TEM cell is connected to port one and the pickup loop to port two of the network analyzer. The pickup loop is positioned at an angle of 45 degrees inside the TEM cell as it is depicted on the right side of Figure 23. Consequently, the pickup loop detects a known fraction, namely  $1/\sqrt{2}$  of the B field inside of the TEM cell. The signal level obtained with the  $s_{21}$  calibration measurement correspond to this detected B field inside of the TEM cell and serves as reference value for comparison with the acquired  $s_{12}$  measurements between the pickup loop and the solenoid RF coil. Since the transmission measurements with the network analyzer are relative measurements the obtained results are scalable to other signal power levels.



## 4. Results

### 4.1 Results SDR Spectrometer

The implemented SDR spectrometer is capable of producing arbitrary shaped RF pulses, blanking and unblanking the custom made RFPA, recording acquired data in a specific time window and controlling rotating gradient fields. Thereby, the RF pulse length and amplitude as well as the readout-length and -delay can be freely chosen. Figure 24 shows the corresponding signals measured with an oscilloscope. In the chosen example, a rect-pulse with an amplitude of 500mV and a length of 200 $\mu$ s was defined in the spectrometer software. The readout delay was set to 80 $\mu$ s and the length of the readout window to 500 $\mu$ s. As it can be seen from the graph in Figure 24, the pulse shape and the specified parameters are accurately created at the corresponding analog RF output channels of the spectrometer. Moreover, the generated blanking pulse (green curve) is nicely synchronized to the RF pulse. Further on, the chosen Larmor frequency of 3.63MHz which is used for the modulation of the rect-pulse is generated precisely and without any distortions. This is demonstrated in Figure 25 which presents a detailed enlargement of the played rect-pulse.

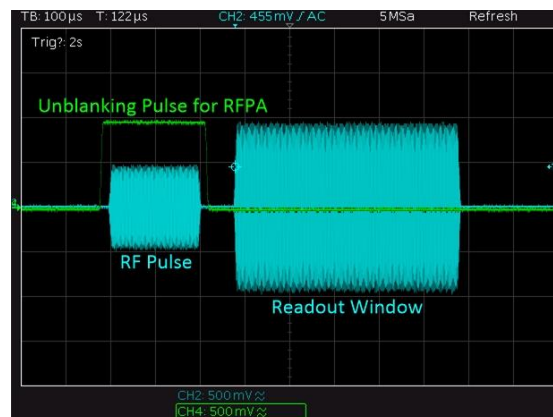


Figure 24: The graphs shows the measured signals produced by the spectrometer when a rect-pulse with an amplitude of 500mV and a length of 200 $\mu$ s, a readout delay of 80 $\mu$ s and a readout length of 500 $\mu$ s was specified in the software.

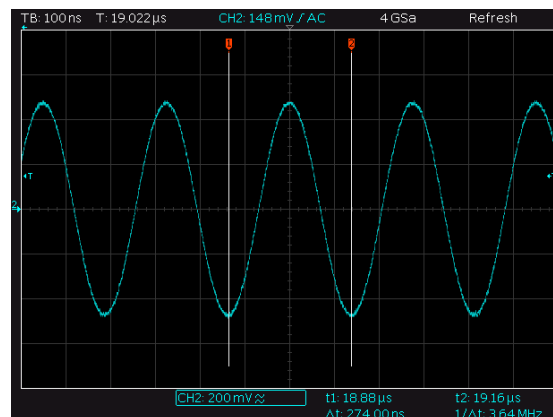


Figure 25: The graph shows a detailed enlargement of the measured rect-pulses generated by the Spectrometer.

In addition to the already presented rect-pulse, the spectrometer also allows to create any conceivable pulse shape. Therefore, the user needs to describe the desired pulse shape through digital samples and load them into the *gated\_vector\_source* block where the RF pulse shape is stored. The pulse shape is described through a mathematical function in a python script and the digital samples of the pulse shape are transferred to the *gated\_vector\_source* block during the initialization phase of the GNU Radio flowgraph. As one possible example for a more complex shaped RF pulse, a sinc-pulse with a maximum amplitude of 200mV and a length of 120 $\mu$ s is presented in Figure 26 a). The representation of the sinc-pulse through digital samples is shown in Figure 26 b).

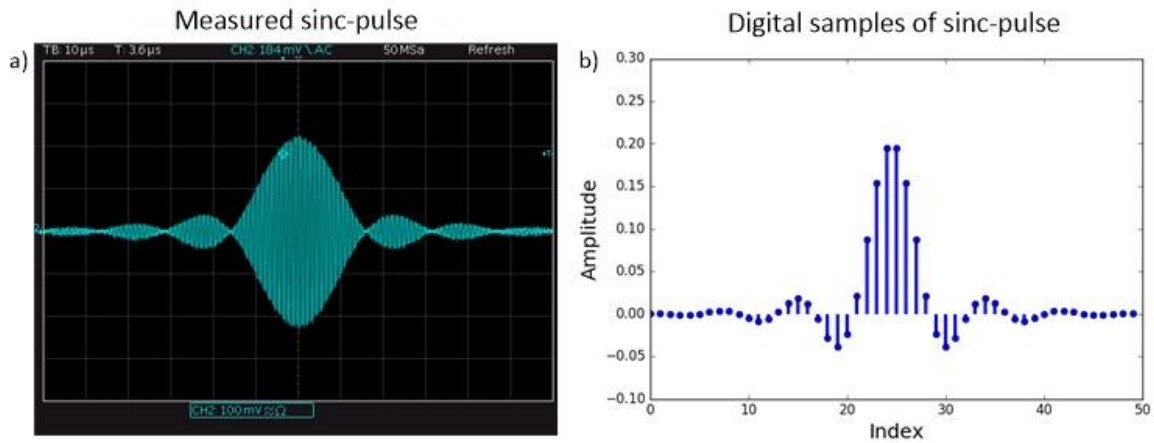


Figure 26: a) The graph shows a measured sinc-pulse with a maximum amplitude of 200mV and a length of 120 $\mu$ s generated by the spectrometer as an example for a more complex shaped RF-pulse. b) Shows the digital representation of the generated sinc-pulse.

Finally, the pulses required to control the stepper motor for the gradient ring rotation are successfully generated at the GPIO pins of the LFTX B daughterboard. The corresponding measured signals are shown in Figure 27. The pulses are with  $\sim 1.50$ ms long enough to allow the detection of the positive pulse edge by the motor-driver. Likewise, the spacing between the pulses is large enough for the motor-driver to distinguish between two consecutive pulses and the pulse amplitude of 3.3V lies above the specified threshold. Theoretically the motor driver is capable of processing control signals with a frequency of up to 60kHz which corresponds to a pulse length of  $\sim 8\mu$ s. The generation of more accurately timed pulses from a python script is not possible. However typical MR imaging experiments have repetition times  $TR > 2$ ms ( $f = 500$ Hz), indicating that the current implementation is fast enough to cover most MR applications. The interface to the motor-driver has been tested. It allowed to accurately turn the stepper motor by a defined angel.

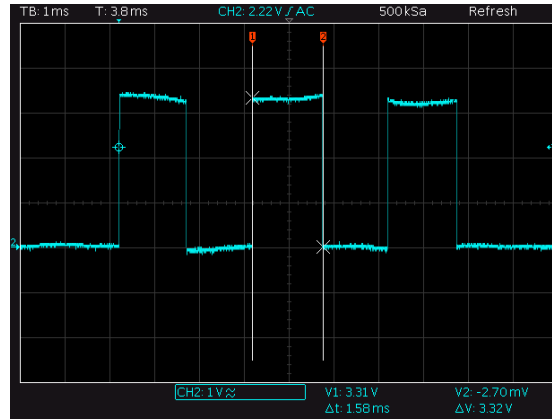


Figure 27: The graph shows 3 pulses produced at the GPIO pins of the LFTX B daughterboard of the spectrometer which are used to control the stepper motor for the gradient ring rotation. The 3 shown positive pulses edges would turn the stepper motor by three angle steps.

In order to also test the receive capabilities of the implemented spectrometer a signal generator was used to generate test signals and mimic the NMR signal. The test signal was inputted to the preamplifier which was connected to the input of the spectrometer. The Larmor frequency was set to 3.63MHz. Figure 28 shows three screenshots of the SDR spectrometer GUI, displaying the received signal at the spectrometer input for the different measurement respectively. For the screenshot in Figure 28 a) the test signal had the same frequency as the specified Larmor frequency (3.63MHz) and an input power of -40dBm. Since the received signals are displayed with respect to the Larmor frequency, horizontal lines are observed indicating a frequency difference of 0Hz. For the screenshots shown in Figure 28 b) and c), the test signal had a frequency of 3.632MHz and an input power of -40dBm. Hence, the signal frequency was 2kHz larger than the specified Larmor frequency. This frequency can be clearly seen in the received signals displayed in the screenshots b) and c). For the measurement in c), the preamplifier at the spectrometer input had been removed which is the reason why the observed signal amplitude in this screenshot is reduced. The difference between the signal amplitude in c) and b) equals 18dB which corresponds to the gain factor of the utilized preamplifier.

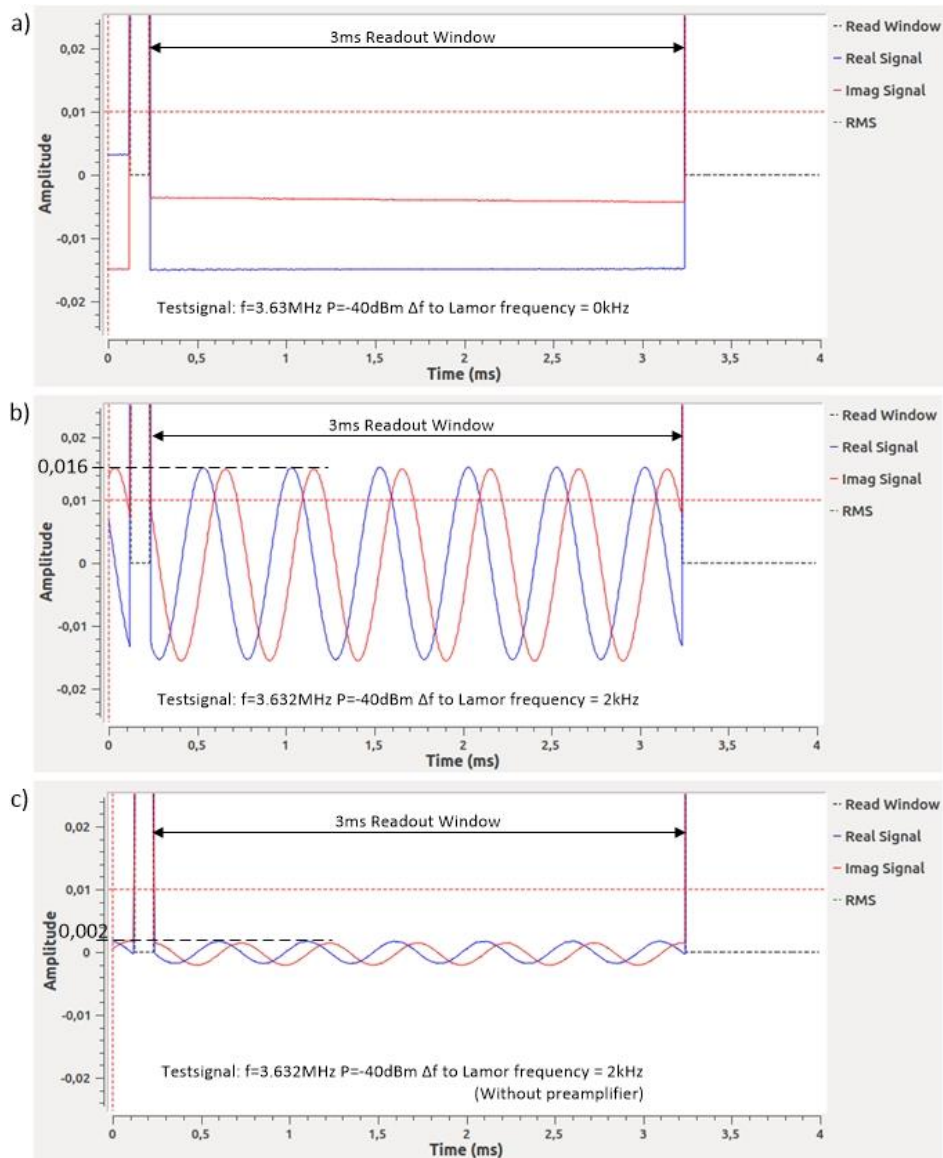


Figure 28: Three Screenshots of the SDR spectrometer GUI displaying the received signals for different test signals in order to mimic the NMR signal at the spectrometer input. The spectrometer was set to a Larmor frequency of  $3.63\text{MHz}$ . The test signals were: a)  $f=3.63\text{MHz}$   $P=-40\text{dBm}$ , b)  $f=3.632\text{MHz}$   $P=-40\text{dBm}$  and c)  $f=3.632\text{MHz}$   $P=-40\text{dBm}$ . For the measurement in c) the preamplifier had been removed.

## 4.2 Results RFPA

### 4.2.1 Output Signal Level Converter

In order to increase the amplitude of the unblanking pulse produced by the spectrometer from  $1\text{V}$  to the required  $3\text{V}$  (TTL level), the level converter presented in chapter 3.3 is used. Figure 29 shows the blanking pulse as it is produced by the spectrometer (blue curve) and after it has passed the level converter (green curve). As it can be seen from the graph, the level converter successfully raises the pulse amplitude from  $1\text{V}$  to  $3\text{V}$ . Further the original pulse shape and length are maintained without changing the slope of the pulse edges. This is important to ensure that the RFPA is unblanked as it is specified by the spectrometer and that the level converter does not introduce any delays.

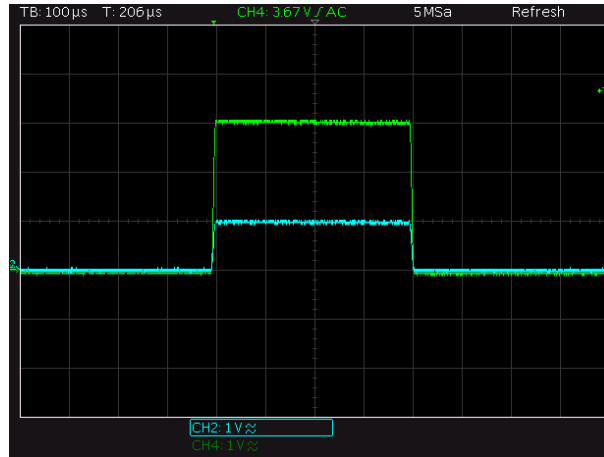


Figure 29: The graph shows the unblanking pulse for the RFPA as it is produced by the spectrometer (blue curve) and after it has passed the level converter (green curve). The amplitude is raised from 1V to 3V by the level converter.

#### 4.2.2 Input Power vs. Output Power

In order to investigate the performance of the RFPA, the output power  $P_{out}$  was measured for a defined input power  $P_{in}$ . Thereby,  $P_{in}$  was increased in steps of 0.5mW starting from 0.5mW until the maximum output power  $P_{max}$  of 1kW was reached. This measurement series was acquired for the different Larmor frequencies of hydrogen at the magnetic field strengths  $B_0 = 0.1T$  (4.3MHz), 0.2T (8.3MHz), 0.3T (12.8MHz), 0.5T (21.3MHz) and 1.0T (42.6MHz). Figure 30 shows the according input power  $P_{in}$  versus output Power  $P_{out}$  plot. Therein, the solid black line indicates the ideal output power curve for a gain factor of 50dB as a reference.

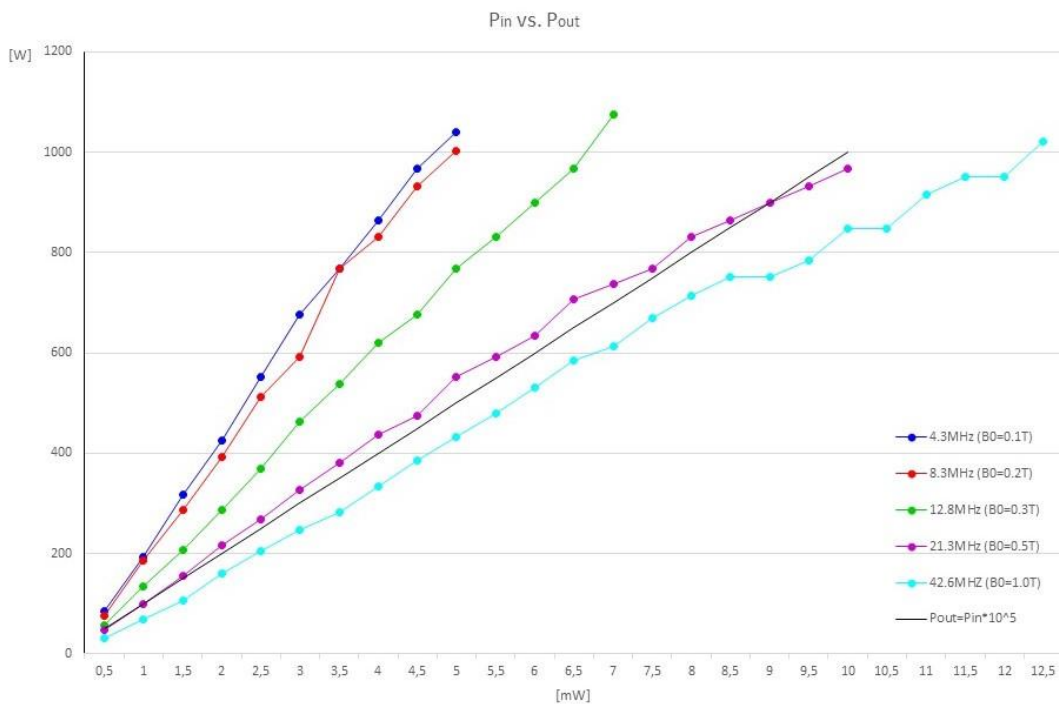


Figure 30: Input power  $P_{in}$  plot versus the output power  $P_{out}$  of the RFPA for the Larmor frequencies of hydrogen at magnetic field strengths  $B_0 = 0.1T$ , 0.2T, 0.3T, 0.5T and 1.0T showing good linearity over the investigated frequency range.

As it can be seen from Figure 30, the RFPA shows good linearity over the investigated frequency range  $f=1.8\text{-}54\text{MHz}$  with a maximum output power level of around  $1\text{kW}$  peak power. Thereby, the utilizable input power range varies depending on the frequency. For lower frequencies ( $4.3\text{MHz}$  and  $8.3\text{MHz}$ ) the maximum output power is reached at an input power of  $5\text{mW}$ . This corresponds to the maximum output of the implemented SDR spectrometer ( $500\text{mV}$  in a  $50\Omega$  system). For higher frequencies ( $42.6\text{MHz}$ ) the RFPA can operate until an input power of  $12.5\text{mW}$ . The utilizable input power range can be easily adapted to the desired range by exchanging the integrated attenuator ( $13\text{dB}$ ) at the RFPA input. This is also necessary in order to protect the RFPA from damage, since the driver stage with a gain of  $33\text{-}34\text{dB}$  would otherwise transmit too much power to the amplification stage and damage the transistor (BLF188XR, NXP, Eindhoven, Netherlands) which is limited to a  $1.2\text{kW}$  maximum power output for the lower frequency range ( $f=2\text{-}30\text{MHz}$ ) [65]. However, this limit could be extended by replacing the current transistor with the succeeding model (MRF1K50H, NXP, Eindhoven, Netherlands) which is dimensioned for a maximum power output of  $1.5\text{kW}$ . Table 1 lists the gain factor of the RFPA in the current setup at different frequencies alongside with the corresponding field strength for proton imaging.

Frequency	Gain factor	Field strength
4.3MHz	53dB	0.1T
8.3MHz	53dB	0.2T
12.8MHz	51dB	0.3T
21.3MHz	50dB	0.5T
42.4MHz	49dB	1.0T

*Table 1: Table lists the gain factor of the RFPA at different frequencies alongside the corresponding field strength for proton imaging.*

### 4.2.3 Amplified RF Pulses

The RFPA successfully amplified rect- and sinc-pulses generated by the implemented SDR spectrometer. Figure 31 exemplarily shows a  $1200\mu\text{s}$  long rect-pulse with an amplitude of  $\sim 500\text{mV}$  (a) and a  $120\mu\text{s}$  long sinc pulse with a maximum amplitude of  $200\text{mV}$  (c) on the left side. On the right side the same pulses are shown after amplification with the RFPA and a  $40\text{dB}$  attenuation (b,d). The  $\sim 500\text{mV}$  amplitude of the rect-pulse leads to an output voltage level of around  $200\text{V}$  which corresponds to a total gain factor of  $52\text{dB}$  and a power level of  $800\text{W}$  in a  $50\Omega$  system. This performance is comparable to power amplifiers used in lower priced clinical MRI systems which provide a similar output power level. The distortions observed at the beginning of the rect-pulse can be addressed by digital pre-distortion techniques when designing the pulse in the digital domain by increasing the pulse amplitude at the beginning of the pulse in steps rather than having an infinitely steep pulse edge.

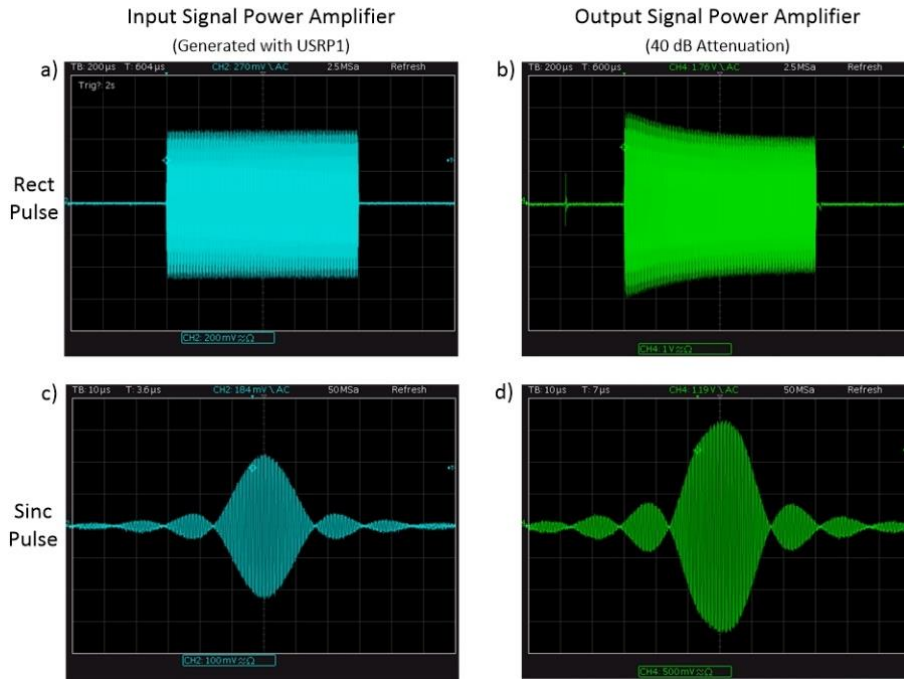


Figure 31: A 1200µs long rect-pulse with an amplitude of 500mV (a) and a 120µs long sinc pulse with a maximum amplitude of 200mV (c) are shown on the left side. Both pulses are generated by the SDR spectrometer. On the right side (b,d) the same pulses are shown after amplification with the RFPA and 40dB attenuation.

## 4.3 Results Solenoid RF Coil

### 4.3.1 $B_1^+$ Field Simulations

To find the suitable geometry of the solenoid RF coil, the length  $L$  and the number of turns  $N$  of the implemented 3D simulation model of the solenoid RF coil were varied between 160mm and 200mm (in steps of 20mm) and 14 and 20 (in steps of 2) respectively. Table 1 lists all parameter combinations that have been simulated and states the resulting maximum inhomogeneity within the sample and the maximum  $B_1^+$  amplitude in the center of the RF coil. The maximum inhomogeneity within the sample was calculated as maximum relative difference from the  $B_1^+$  value in the RF coil center along the RF coils central axis.

Parameter Combination	Max. $B_1^+$ Field Inhomogeneity	$B_1^+$ Amplitude in Coil Center [ $\mu\text{T}/\sqrt{kW}$ ]
L=160mm, N=16	7.3%	1698
L=180mm, N=18	4.7%	2042
L=200mm, N=20	3.4%	2694
L=200mm, N=14	3.4%	1374
L=200mm, N=16	3.4%	1455
L=200mm, N=18	3.4%	1917

Table 2: The table shows the different parameter combination for the length  $L$  and the number of turns for the coil that were simulated.



From Table 1 it can be seen that the homogeneity within the spherical sample increases with the length of the solenoid RF coil while it is independent from the number of turns<sup>3</sup>. The number of turns only affects the  $B_1^+$  field amplitude in the center of the RF coil. The closer the spacing between the individual turns of the solenoid RF coil is the higher the value.

As final design the solenoid RF coil with a length of 200mm and 20 windings was chosen. This design achieves with 3.4% the best homogeneity and has with 2694 in  $\mu\text{T}/\sqrt{\text{kW}}$  the highest  $B_1^+$  field amplitude in the RF coil center. Extension of the RF coil would improve the homogeneity even further, however this would also increase the length of the electrical conductor which increases RF coil resistance and therefore decreases signal to noise ratio. Similarly, a higher number of turns would further increase the  $B_1^+$  amplitude in the coil center but also decreases the spacing between the individual turns which results in an increased RF resistance through the proximity effect [66]. The center-to-center distance of 10mm between adjacent windings was considered to be a good tradeoff and is in line with the coil design presented in [17].

Figure 32 shows the vector field of the magnetic (H) field (a) and the electric (E) field (b) of the final solenoid RF coil design. In the coordinate system of Figure 32, the main magnetic field  $B_0$  of the Halbach magnet is pointing in the z-direction so that the solenoid RF coil design allows the application of an RF pulse perpendicular to the main magnetic field.

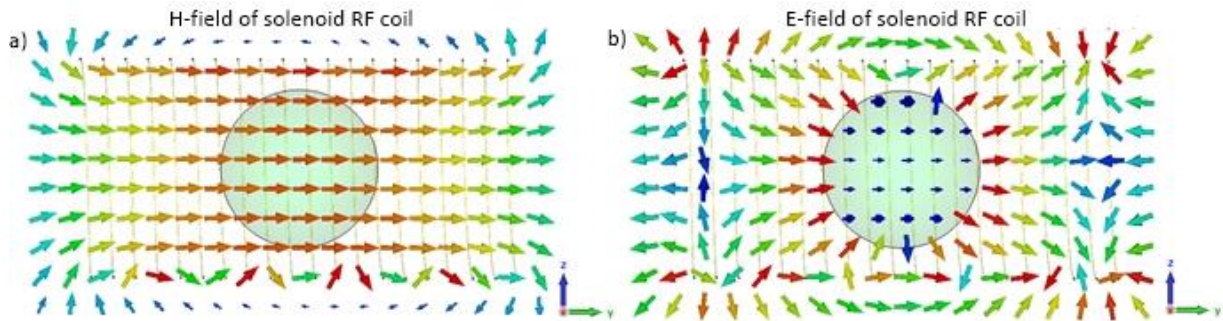


Figure 32: Vector field of H-field (a) and E-field (b) (same phase) of the final solenoid RF coil design ( $L=200\text{mm}$ ,  $N=20$ ).

Figure 33 shows the magnitude of the simulated  $B_1^+$  field in  $\mu\text{T}/\sqrt{\text{kW}}$  in the transversal plane (zy-plane) of the RF coil for the parameter combinations  $L=160\text{mm}$ ,  $N=16$  (a),  $L=200\text{mm}$ ,  $N=16$  (b) and  $L=200\text{mm}$ ,  $N=20$  (c) respectively. The black circle marks the outline of the spherical sample in the coil center. A visual comparison confirms that for a solenoid RF coil of same length ( $L=200\text{mm}$  b, c), the  $B_1^+$  field values increase with higher number of turns ( $N=20$  (c)  $>$   $N=16$  (b)). Likewise, the homogeneity within the sample improves with the length of the solenoid RF coil ( $L=160\text{mm}$  a  $<$   $L=200\text{mm}$  b) for a design with the same number of turns ( $N=16$  a, b).

<sup>3</sup> This independence of the  $B_1^+$  field homogeneity from the coils number of turns was the reason why different windings were only simulated for one coil length ( $L=200\text{mm}$ ).



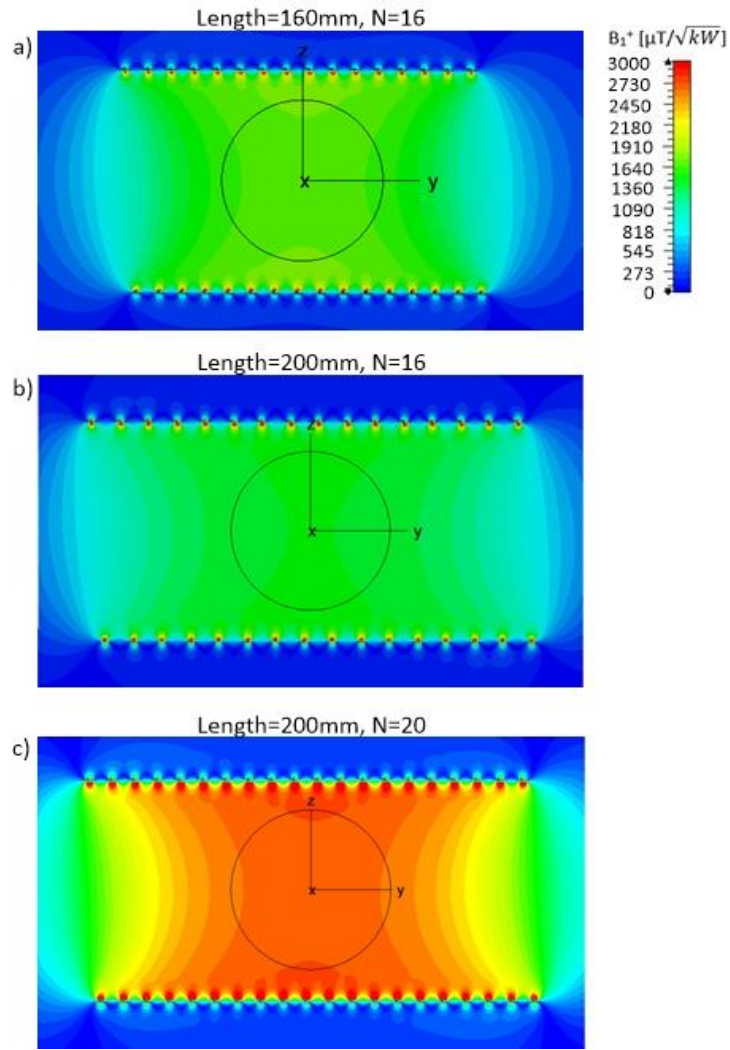


Figure 33: The graphs show the magnitude of the simulated  $B_1^+$  field distribution in the transversal plane (zy-plane) of the RF coil for the parameter combinations  $L=160\text{mm}$ ,  $N=16$  (a),  $L=200\text{mm}$ ,  $N=16$  (b) and  $L=200\text{mm}$ ,  $N=20$  (c).

Finally, Figure 34 shows the  $B_1^+$ -field magnitude inside the sample along straight lines through the center of the coil in the x-, y-, and z-direction. As it can be seen, the field inhomogeneities within the sample volume are smaller than 3.43%. In the transversal cross-section the homogeneity is even better with a maximum difference of 1.39%.

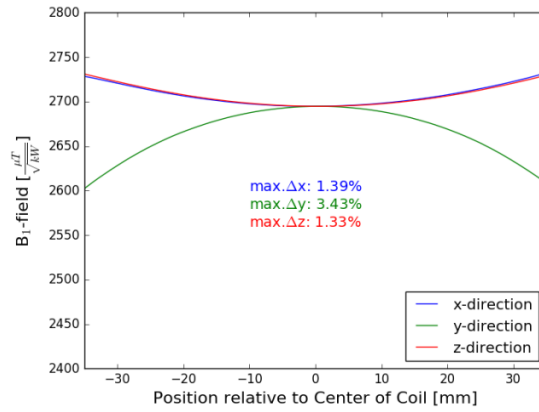


Figure 34: The graph shows the  $B_1^+$  field values inside the sample along straight lines through the coil center in the x-, y- and z-direction respectively.

### 4.3.2 Construction

The final RF coil design obtained by the electromagnetic field simulations was constructed. It consists of 20 windings, is 200mm long and has an inner diameter of 96mm. In order to be able to realize the simulated geometry as accurately as possible, a 3D CAD model of a 200mm long cylinder (wall thickness = 3mm, inner diameter = 89.15mm) with a 0.45mm spiral cavity to position the wire (diameter = 0.85mm) was designed and 3D printed in ABS. AWG 20 copper wire was wound around the cylinder guided by the cavity. The finished solenoid RF coil is shown in Figure 35 a). As a tuning and matching circuit a parallel tuning capacitor and a series matching capacitor were used. The tuning capacitance consists of a nonmagnetic, fixed capacitor (33 pF, Voltronics, Cazenovia, USA) in parallel with a nonmagnetic trim capacitor (1 pF-40 pF, Voltronics, Cazenovia, USA). For matching an adjustable, nonmagnetic trim capacitor (1 pF-40 pF, Voltronics, Cazenovia, USA) is sufficient. The final tuning matching circuit is displayed in Figure 35 b). This setup allows to tune and match the solenoid RF coil to the intended center frequency of 3.63MHz of the Halbach prototype magnet. To connect the RF coil to the T/R-switch a standard coaxial cable with a BNC connector at one end is used. The total material costs for the RF coil are ~100€. The costs could be further reduced by replacing the expensive non-magnetic trim capacitors by cheaper trim capacitors that are magnetic. This is possible since the tuning and matching circuit is positioned outside of the magnetic field of the Halbach magnet ( $B_{\text{outside}} \approx 0$ ).

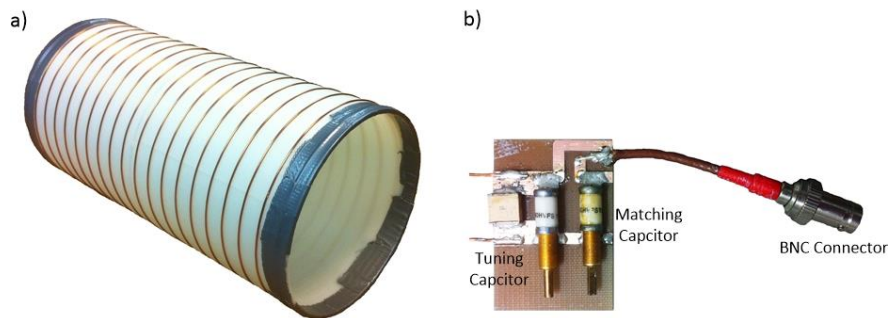


Figure 35: a) Picture of the finished solenoid RF coil (length 200 mm, number of turns 20) wound on a 3D printed cylinder. b) Picture of the tuning and matching circuit.

### 4.3.3 Bench Measurement

The finished RF solenoid coil was tested and characterized for a loaded and unloaded scenario by an  $S_{11}$  reflection measurement with a network analyzer. The obtained results are presented in Figure 36. As it can be seen, the RF coil is well tuned to the desired resonance frequency of 3.63MHz and the impedance matching is in both cases better than -40dB. For the unloaded RF coil a -3dB bandwidth of 38.42kHz was measured which results in a Q-factor of 188.97. For the loaded case the bandwidth and the corresponding Q-factor are 46.97kHz and 154.56 respectively. This leads to a Q-factor ratio  $Q_{\text{loaded}}/Q_{\text{unloaded}}$  of 0.82 which indicates that the losses in the RF coil dominate over the losses in the sample. This was expected since the coupling between the RF coil and the sample is generally lower at such low frequencies [58]. Moreover, the measured bandwidth of the RF coil is relatively large compared to other RF coil designs which increases also the noise bandwidth during signal reception. However, the large bandwidth is required during the transmission phase in order to excite a broader frequency range to satisfy the inhomogeneity of the main magnetic field using the projection method. The measured bandwidth of 46.97kHz of the loaded RF coil incorporates magnetic field inhomogeneities of up to 0.56mT with respect to the designated center field strength of 85mT of the prototype Halbach magnet.

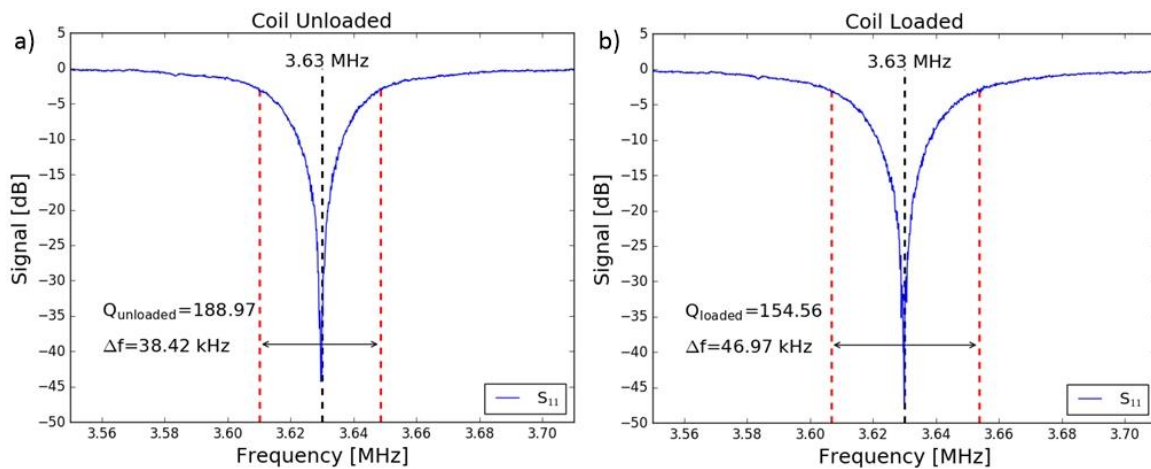


Figure 36:  $S_{11}$  reflection measurement of solenoid coil for unloaded (a) and loaded (b) case.

### 4.3.4 Measured $B_1^+$ Field

The  $B_1^+$  field produced by the solenoid RF coil was measured with  $s_{12}$  measurements with a network analyzer between the solenoid RF coil and a small pickup loop that was calibrated in the known B field of a TEM cell and positioned along a straight line at one end of the solenoid RF coil. Figure 37 shows the  $s_{21}$  calibration measurement of the pickup loop inside of the TEM cell (black curve) and the  $s_{12}$  measurements between the pickup loop and the solenoid RF coil for the measurements positions of

-50mm (blue curve), 0mm (green curve) and 50mm (red curve) with respect to the central axis of the solenoid RF coil.

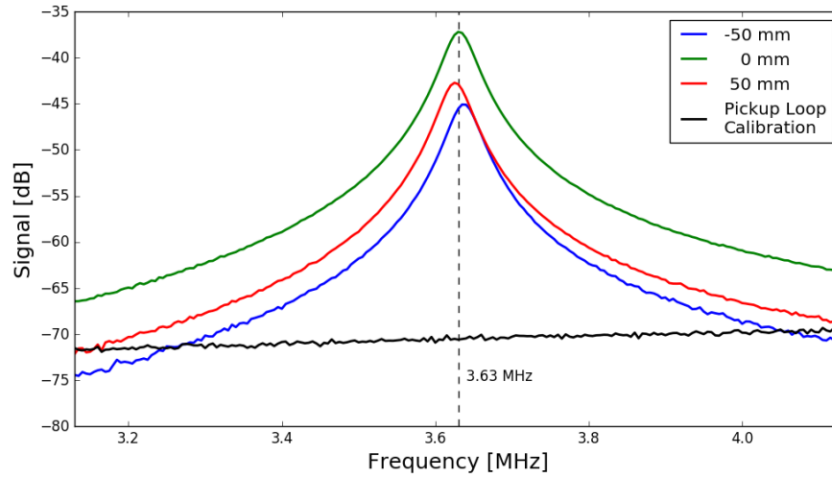


Figure 37: colored curves:  $S_{12}$  measurements between the solenoid coil and the pickup loop; black curve:  $S_{21}$  measurement between pickup loop and TEM cell for calibration of pickup loop.

For the pickup loop calibration measurement (black curve Figure 37) it can be seen that at a frequency of 3.63MHz<sup>4</sup> the B field detected by the pickup loop leads to a signal level of about -70dB. This value serves as the reference for comparison with the acquired  $s_{12}$  measurements between the pickup loop and the solenoid RF coil. The  $s_{12}$  measurements between the solenoid RF coil and the pickup loop (blue, green and red curves Figure 37) result in signal levels between -35dB and -45dB. Hence, the signal levels are between 25dB and 35dB higher than the reference value. This means that the  $B_1^+$  field produced by the solenoid coil at the corresponding position of the pickup loop is by this difference larger than the B field detected by the pickup loop during the calibration measurement inside of the TEM cell. By calculating the B field inside of the TEM cell using the equations (5) and (6), multiplying the result with a factor<sup>5</sup> of  $1/\sqrt{2}$  and scaling it according to the difference, the  $B_1^+$  amplitude of the solenoid RF coils' field can be determined. Figure 38 shows the measured  $B_1^+$  values in  $\mu\text{T}$  generated by the solenoid RF coil along the measurement path for an RF input signal with a frequency of 3.63MHz and a power level of 945W as it was used in the electromagnetic field simulations of the solenoid RF coil.

<sup>4</sup> 3.63MHz is the frequency used in the RF coil simulations. Measurements at this frequency allow comparison between the measurements and the simulations later on.

<sup>5</sup> The factor of  $1/\sqrt{2}$  is necessary since the pickup loop detected only this fraction of the B field inside of the TEM cell during the calibration measurement due to the 45 degree insertion angel.

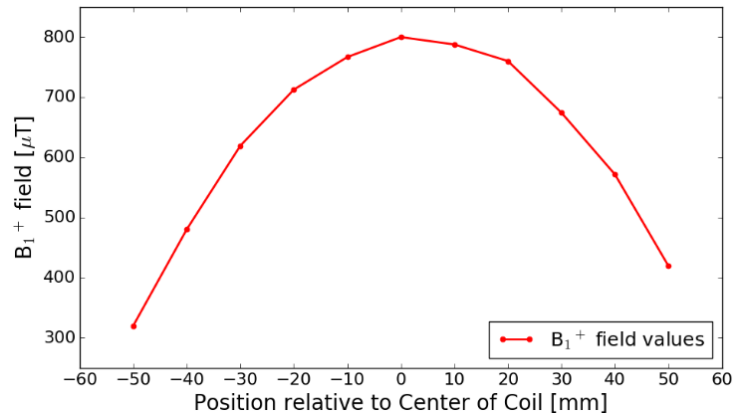


Figure 38: Measured  $B_1^+$  field values generated by the solenoid RF coil along a straight line at one end of the RF coil.

#### 4.3.5 Comparison of Measured and Simulated $B_1^+$ Field

Figure 39 shows a comparison between the simulated and the measured  $B_1^+$  field generated by the RF solenoid coil along a straight line at one end of the RF coil. For the comparison the simulation was used as reference. The graph on the left side shows the absolute  $B_1^+$  field values in  $\mu\text{T}$ . The mean difference between validation measurement and simulation is  $-5.1 \pm 4.2\%$ . The maximum difference is  $-10\%$ . The graph on the right shows the values normalized to the maximum. Here the mean difference is  $-1.2 \pm 4.5\%$  with a maximum relative difference of  $12.5\%$ . The observed differences between measurements and simulations are acceptable considering that the simulations do not incorporate any RF losses in the connecting wires between the RF coil and the tuning and matching circuit as well as the RF losses in the circuit itself. Therefore, the proposed measurement approach allows a low cost validation of the performed RF coil simulations at such low frequencies without using more expensive E- or H-field sensors.

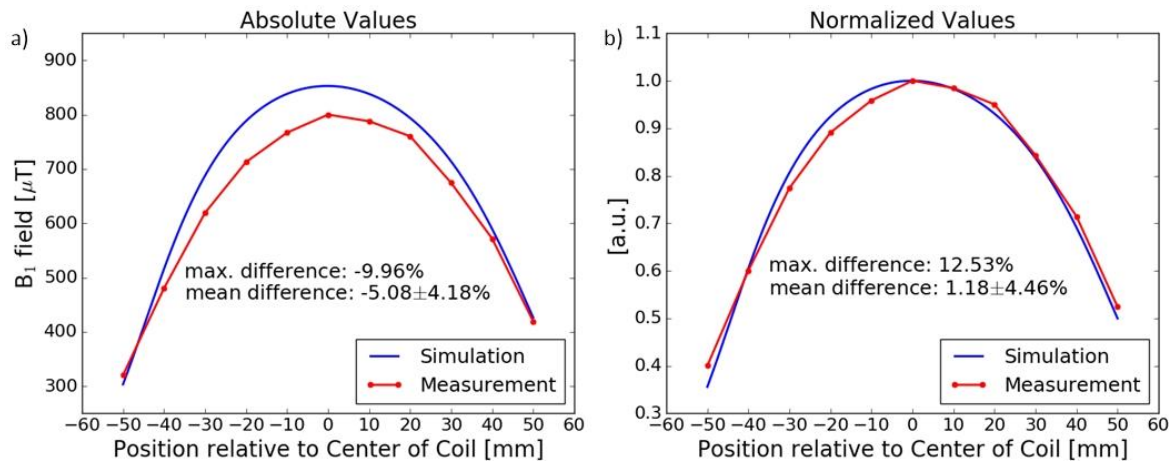


Figure 39: a) Comparison of absolute values between measured and simulated  $B_1$  field of solenoid coil. b) Comparison of to the maximum normalized values between measured and simulated  $B_1$  field of solenoid coil.

## 4.4 Complete MR Transmission/Reception System

The photograph in Figure 40 shows the complete MR transmission and reception system consisting of the SDR spectrometer, the RFPA, the transmit/receive RF coil, the T/R switch and the preamplifier. The whole system occupies a volume of around  $(50 \times 70 \times 30) \text{ cm}^3$ . The total cost were approximately 3000€ (SDR: 1000€; RFPA: 1500€; T/R-Switch: 370€; LNA: 20€; RF coil: 100€).

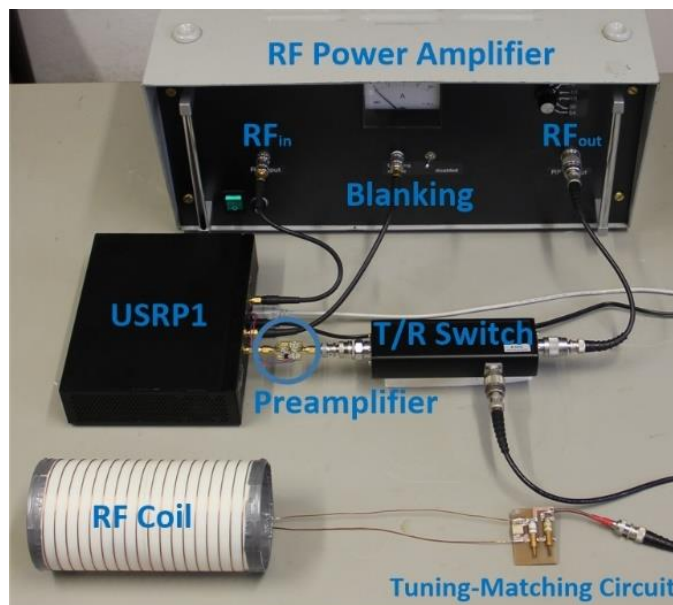


Figure 40: Photograph of the complete MR transmission and reception system consisting of the SDR spectrometer (USRP1), the RFPA, the transmit/receive RF coil, the T/R switch and the preamplifier.

## 5. Discussion and Conclusion

In this master thesis a transmission and reception system was developed for an affordable open source MR system. Results show that the implemented SDR spectrometer is capable of producing arbitrary shaped RF pulses and recording the acquired MR-signal in a user defined time window. The RF pulse length and amplitude as well as the readout-length and –delay can be chosen freely. The spectrometer successfully interfaces with a custom made RFPA, performs blanking/unblanking functions and in this configuration allows a total maximum peak power output of 1kW. This allows for a total  $B_1^+$  amplitude of 2694 $\mu$ T generated by the designed and constructed transmit/receive RF coil which can be utilized for MR applications. Moreover, the SDR allows to control a stepper motor for gradient field rotations by utilizing the available GPIO pins. All design files with respect to this work will be made available under the open source hardware license CERN OHL v1.2 on [www.opensourceimaging.org](http://www.opensourceimaging.org). In summary, the implemented transmission and reception system meets all the necessary requirements to be used for MR imaging experiments, is affordable and due to its open source nature can be reproduced by the community.

The whole system is built on modularity, allowing to replace individual components. The major advantage of utilizing a GNU Radio compatible SDR as a MR spectrometer is that no circuit board development and FPGA programming are needed. Instead, the programming of MR pulse sequences or imaging techniques can be accomplished within an open source software framework like gr-MRI [39]. In an open source development approach of a complex machine like an MRI, this permits that some researchers and developers can work on the implementation of new imaging techniques in software while others can focus on the design of new hardware such as an SDR tailored for the needs in MRI that e.g. provides more RF receive channels.

The USRP1 SDR board utilized in this work has 12 bit ADCs and 14 bit DACs. This is within the range of other MR spectrometers which typically feature a resolution between 12 and 16 bits [67]. The used transmit and receive daughterboards (LFTX and LFRX) allow a maximum Larmor frequency of 30MHz which corresponds to a maximum field strength of 0.7T for proton imaging. However, an extension to higher frequencies could be achieved by replacing the LFTX and LFRX daughterboards with the BasicTX [68] and BasicRX [69] boards which provide an operation frequency range from 1-250MHz but do not feature local oscillators for signal up- and down conversion. Hence, additional analog front end circuits are necessary in order to convert the RF signals from and to the baseband ( $f \leq 32$ MHz) where they can be processed by the ADCs and DACS respectively without violating the sampling theorem.

Another consideration is the temporal resolution of the digital samples in the baseband and readout bandwidth of the SDR spectrometer. Those parameters are directly dictated by the host sampling rate

between the computer and the SDR. In the current setup, a sampling rate of 250kHz is used so that the temporal resolution is 4 $\mu$ s and the readout bandwidth 125kHz. However, the USRP1 provides a host sampling rate of up to 8MS/s which corresponds to a resolution of 125ns and a bandwidth of 4MHz. With this performance the SDR spectrometer lies well within the range of commercial spectrometers which typically feature a resolution between 4 and 10 $\mu$ s.

To further improve the existing spectrometer design, a new customized GNU Radio signal processing block is required that enables the manipulation of the GPIO pins on the daughterboards. Such a block allows to generate the unblanking pulse for the RFPA with the digital pins, freeing one of the analog RF transmission channels. Likewise, the pulse generation for the stepper motor control could be realized within the flowgraph, enabling even shorter and more accurately timed pulses.

The open source custom made RFPA successfully amplified rect- and sinc-pulses produced by the SDR spectrometer up to a maximum output power of 1kW (peak). Hence, the performance of the RFPA is comparable to the performance of lower priced clinical MR scanners. The observed and expected distortions of the amplified rect-pulses can be addressed by digital pre-distortion techniques when designing the RF-pulse. One option to do this is to increase the amplitude of the digital samples at the beginning of the pulse in steps instead of directly jumping to the final pulse amplitude. Furthermore, the input- versus output-power plot showed good linearity over the investigated frequency range. Only the gain factor of the RFPA is dependent on the frequency of the input signal. At lower frequencies the maximum output power is reached faster compared to higher frequencies. However, with the attenuator at the RFPA input it was possible to adapt the RFPA to the output power range of the SDR spectrometer (0-500mV) at the designated Larmor frequency of the COSY MR-scanner. By exchanging the attenuator, the RFPA could be easily adapted to the output range of a different spectrometer or to another operation frequency for the given input range of the SDR spectrometer.

The simulated and constructed RF solenoid coil is 200mm long, has a diameter of 96mm and consist of 20 windings. Hence, it is large enough to place a human hand inside. The simulations revealed that the  $B_1^+$  field homogeneity within the spherical sample is greater than 96.6% and the RF coil provides a  $B_1^+$  field amplitude of 2694  $\mu$ T/ $\sqrt{\text{kW}}$  in the RF coil center. The simulations were validated via  $S_{12}$  measurements with a network analyzer between the RF coil and a small pickup loop that was calibrated in the known B field of a TEM cell. This approach allows a low cost validation of RF coil simulations at such low frequencies without using costly E- or H-field sensors. The comparison between the simulation and the measurement revealed a maximum difference of -10%. Using this difference to estimate the additional power losses in the constructed RF coil compared to the simulations, the constructed RF coil is able produce a  $B_1^+$  field amplitude of 2424 $\mu$ T in the coil center for the maximum output power (1kW) of the RFPA. To further improve the existing RF coil design, the copper wire



utilized as electrical conductor could be replaced by a copper tube which has two advantages. First, due to the skin effect [59], the larger conductor surface of a tube reduces the RF resistance. Second, there is no copper material inside of the conductor that could cause unnecessary thermal noise. Both of these improvements increase the signal to noise ratio during the signal reception [63].

Overall, the SDR spectrometer, the RFPA, the RF solenoid coil and the commercial T/R switch and preamplifier make an affordable (<3000€) transmission and reception system for MR systems with a rotating permanent gradient. The costs have not been optimized and can be decreased further. As soon as the first prototype magnet for the COSI project is finished, it can be used to acquire a first free induction decay (FID) signal. Likewise, the projection method for the generation of 2D images can be tested when the gradient ring and the mechanical system for the rotation are completed. The developed transmission/reception system can be used in a frequency range from 1.8MHz to 30MHz (0.042-0.7T) and is extendable to a frequency of up to 54MHz (1.27T) by exchanging the daughterboards of the SDR board. Adding a second SDR allows the generation of traditional gradient pulses so that the system could potentially also be used in a common MRI system. Future work in the transmit/receive system should focus on removing system components that are not open source yet, such as the T/R switch. For the implementation of a suitable open source T/R switch, a quarter lambda transformation in combination with a set of crossed diodes could be utilized. Such a configuration allows to alternately present a high input impedance and a very low input impedance at the connecting port of the preamplifier during the respective transmit- and receive-phase.

The implemented transmission/reception system presented in this master thesis is an important step on the roadmap of the COSI project to an affordable, open source MR system. Its modular structure provides a firm basis for future research and allows to use the individual system parts in the context of other projects. It is therefore a contribution to address the issue of unequal access to MR for many patients around the world.

## References

1. TWO VIEWS. *quick MRI history*. [cited 2016 9. Nov.]; Available from: <http://www.two-views.com/mri-imaging/history.html#sthash.NSSGMgKe.aywiqXba.dpbs>.
2. Oppelt, A., *Imaging systems for medical diagnostics*. 2005, Erlangen: Publicis.
3. Sferrella, S. *Equipment Service: Total Cost of Ownership*. 2012 [cited 2016 15. Nov.]; Available from: <http://www.radiologybusiness.com/topics/business/equipment-service-total-cost-ownership>.
4. Winter, L. *Open Source Imaging Initiative (OSI<sup>2</sup>)*. in *World Health Summit*. 2016.
5. World Health Organization (WHO). *Essential Health Technologies: Medical Equipment - Data by Country*. [cited 2016, 8. Nov.]; Available from: [http://gamapserver.who.int/gho/interactive\\_charts/health\\_technologies/medical\\_equipment/atlas.html](http://gamapserver.who.int/gho/interactive_charts/health_technologies/medical_equipment/atlas.html).
6. Winter, L., et al., *Open Source Imaging Initiative*, in *Proc Intl Soc Mag Reson Med*. 2016. p. 1396.
7. Breitenheiser, M.J., et al., *Radiologically occult scaphoid and wrist fractures. Preliminary results in comparison of 0.2-T and 1.0-T units*. *Der Radiologe*, 1997. **37**(10): p. 812-818.
8. Ejbjerg, B.J., et al., *Optimised, low cost, low field dedicated extremity MRI is highly specific and sensitive for synovitis and bone erosions in rheumatoid arthritis wrist and finger joints: comparison with conventional high field MRI and radiography*. *Annals of the rheumatic diseases*, 2005. **64**(9): p. 1280-1287.
9. Kladny, B., et al., *Comparison of low-field (0.2 Tesla) and high-field (1.5 Tesla) magnetic resonance imaging of the knee joint*. *Archives of orthopaedic and trauma surgery*, 1995. **114**(5): p. 281-286.
10. Merl, T., et al., *Results of a prospective multicenter study for evaluation of the diagnostic quality of an open whole-body low-field MRI unit. A comparison with high-field MRI measured by the applicable gold standard*. *European Journal of Radiology*, 1999. **30**(1): p. 43-53.
11. Pääkkö, E., et al., *Low-field versus high-field MRI in diagnosing breast disorders*. *European Radiology*, 2005. **15**(7): p. 1361-1368.
12. Parizel, P.M., et al., *Low-field versus high-field MR imaging of the knee: a comparison of signal behaviour and diagnostic performance*. *European Journal of Radiology*, 1995. **19**(2): p. 132-138.
13. Savnik, A., et al., *MRI of the arthritic small joints: comparison of extremity MRI (0.2T) vs. high-field MRI (1.5T)*. *Eur Radiol*, 2001. **11**(6): p. 1030-1038.
14. Shellock, F.G., et al., *Evaluation of the rotator cuff and glenoid labrum using a 0.2-Tesla extremity magnetic resonance (MR) system: MR results compared to surgical findings*. *J Magn Reson Imaging*, 2001. **14**(6): p. 763-770.
15. Zangos, S., et al., *MR-guided transgluteal biopsies with an open low-field system in patients with clinically suspected prostate cancer: technique and preliminary results*. *European Radiology*, 2005. **15**(1): p. 174-82.
16. Winter, L., et al., *COSI Magnet: Halbach Magnet and Halbach Gradient Designs for Open Source Low Cost MRI*, in *Proc Intl Soc Mag Reson Med*. 2016. p. 3568.
17. Cooley C.Z., et al., *Two-Dimensional Imaging in a Lightweight Portable MRI Scanner without Gradient Coils*. *Magnetic Resonance in Medicine*, 2015. **73**: p. 872-883.
18. Blümler, P., *Permanent Magnet System for MRI with Constant Gradient mechanically adjustable in Direction and Strength*. *Concept in Magnetic Resonance B: MR Engineering*, 2015: p. 12.
19. magritek. *Kea NMR and MRI Spectrometer Consoles*. [cited 2016 14. Nov.]; Available from: <http://www.magritek.com/products/kea/>.
20. Oxford Instruments. *MARAN Ultra*. [cited 2016 14. Nov.]; Available from: <https://www.oxford-instruments.com/products/analysers/stationary-benchtop-analyser/maran-ultra>.

21. Pure Devices GmbH. *Research MRI System*. [cited 2016 15. Nov.]; Available from: <http://www.pure-devices.com/index.php/products/products-research/products-research-overview.html>.
22. Haacke, E.M., *Magnetic resonance imaging*. 1999, New York: Wiley.
23. Reiser, M., W. Semmler, and H. Hricak, *Magnetic resonance tomography*. 2008, Berlin: Springer.
24. Dössel, O., *Bildgebende Verfahren in der Medizin: Von der Technik zur medizinischen Anwendung*. 2000, Berlin, Heidelberg: Springer.
25. Lauterbur, P.C., *Image formation by induced local interactions: Examples employing nuclear magnetic resonance*. *Nature*, 1973. **242**(5394): p. 190-191.
26. Halbach, K., *Design of Permanent Multipole Magnets with Oriented Rare Earth Cobalt Materials*, in *Nuclear Instruments and Methods*. 1980.
27. H. Raich, P.B., *Design and Construction of a Dipolar Halbach Array with a Homogeneous Field from Identical Bar Magnets: NMR Mandhalas*. 2004. p. 16-25.
28. Soltner, H. and P. Blümli, *Dipolar Halbach magnet stacks made from identically shaped permanent magnets for magnetic resonance*, in *Concepts in Magnetic Resonance Part A*. 2010. p. 211-222.
29. Michal, C.A., *A low-cost spectrometer for NMR measurements in the Earth's magnetic field*. *Measurement Science and Technology*, 2010. **21**(10): p. 105902.
30. Asfour, A., K. Raoof, and J.-P. Yonnet, *Software Defined Radio (SDR) and Direct Digital Synthesizer (DDS) for NMR/MRI Instruments at Low-Field*. *Sensors*, 2013. **13**(12): p. 16245–16262.
31. Jie, S., et al., *Home-built magnetic resonance imaging system (0.3 T) with a complete digital spectrometer*. *Review of Scientific Instruments*, 2005. **76**(10): p. 105101.
32. Gengying, L., et al., *Digital nuclear magnetic resonance spectrometer*. *Review of Scientific Instruments*, 2001. **72**(12): p. 4460.
33. Peng, W.K., L. Chen, and J. Han, *Development of miniaturized, portable magnetic resonance relaxometry system for point-of-care medical diagnosis*. *Review of Scientific Instruments*, 2012. **83**(9): p. 095115.
34. Parnell, S.R., et al., *Digital pulsed NMR spectrometer for nuclear spin-polarized  $^3\text{He}$  and other hyperpolarized gases*. *Measurement Science and Technology*, 2008. **19**(4): p. 045601.
35. Takeda, K., *A highly integrated FPGA-based nuclear magnetic resonance spectrometer*. *Rev. Sci. Instrum.*, 2007. **78**(3): p. 033103.
36. Takeda, K., *OPENCORE NMR: Open-source core modules for implementing an integrated FPGA-based NMR spectrometer*. *Journal of Magnetic Resonance*, 2008. **192**(2): p. 218–229.
37. Tang, W. and W. Wang, *A single-board NMR spectrometer based on a software defined radio architecture*. *Meas. Sci. Technol.*, 2011. **22**(1): p. 015902.
38. Chen, H.-Y., et al., *An ultra-low cost NMR device with arbitrary pulse programming*. *Journal of Magnetic Resonance*, 2015. **255**: p. 100–105.
39. Hasselwander, C.J., Z. Cao, and W.A. Grissom, *gr-MRI: A software package for magnetic resonance imaging using software defined radios*, in *Journal of Magnetic Resonance*. 2016. p. 47-55.
40. The GNU Radio Foundation. *GNU Radio - The Free & Open Software Radio Ecosystem*. [cited 2016 4. Nov.]; Available from: <http://gnuradio.org/>.
41. Holland, O., H. Bogucka, and A. Medeisis, *Opportunistic spectrum sharing and white space access*. Wiley.
42. Nagel, S., *Portable Waveform Development for Software Defined Radios*. 26. Mai 2011, Karlsruher Instituts für Technologie: Karlsruhe.
43. Gadgets, G.S., *an open source SDR platform*, in *HackRF One*, G.S. Gadgets, Editor.
44. StemLabs. *Red Pitaya*. [cited 2016 18. Oct.]; Available from: <http://redpitaya.com/>.
45. Ettus Research. *USRP B200/B210 Bus Series*. [cited 2016 2. Nov.]; Available from: [https://www.ettus.com/content/files/b200-b210\\_spec\\_sheet.pdf](https://www.ettus.com/content/files/b200-b210_spec_sheet.pdf).

46. CORPORATION, P.V., *Discover the world's most versatile software defined wireless platform*, in *Crimson TNG*.
47. Ettus Research. *USRP1*. [cited 2016 18. Oct.]; Available from: <https://www.ettus.com/product/details/USRPPKG>.
48. Fernando Pérez, B.E.G., *IPython: A System for Interactive Scientific Computing*. Computing in Science & Engineering, 2007. **9**(3): p. 21-29.
49. Ettus Research. *LFTX Daughterboard 0-30MHz*. [cited 2016 4. Nov]; Available from: <https://www.ettus.com/product/details/LFTX>.
50. Ettus Research. *LFRX Daughterboard 0-30MHz*. [cited 2016 4. Nov]; Available from: <https://www.ettus.com/product/details/LFRX>.
51. Scott, G.C., *MRI Transmitter Amplifier Systems*, in *Proc Intl Soc Mag Reson Med*. 2012. p. 8343.
52. RFP. *HF 1000 RF PALLET 1KW 1.5-35 MHz* [cited 2016 4. Nov.]; Available from: <http://www.italab.it/uploads/prodotti/DATA3.pdf>.
53. RFP. *HF 1000 BX*. [cited 2016 4. Nov.]; Available from: [http://www.italab.it/uploads/prodotti/HF\\_1000\\_BX\\_\(2\)1.pdf](http://www.italab.it/uploads/prodotti/HF_1000_BX_(2)1.pdf).
54. FUNK Amateur. *Bausatz für QRP-Linear-Endstufe nach DL2EWN*. [cited 2016 4. Nov.]; Available from: [http://www.box73.de/product\\_info.php?products\\_id=1899&XTCSid=86316710323ff4cb4d6e8857b9a31277](http://www.box73.de/product_info.php?products_id=1899&XTCSid=86316710323ff4cb4d6e8857b9a31277).
55. W6PQL. *A 1 KW SSPA for 1.8-54MHz*. [cited 2016 4. Nov.]; Available from: [http://www.w6pql.com/1\\_kw\\_sspa\\_for\\_1\\_8-54\\_mhz.htm](http://www.w6pql.com/1_kw_sspa_for_1_8-54_mhz.htm).
56. W6PQL. *A 1.5 KW Low Pass Filter for 160-6 Meters*. [cited 2016 4. Nov.]; Available from: [http://www.w6pql.com/a\\_1.5kw\\_lpf\\_for\\_160-6m.htm](http://www.w6pql.com/a_1.5kw_lpf_for_160-6m.htm).
57. NMR Service GmbH. *Duplexer/TR Schalter*. [cited 2016 9. Nov.]; Available from: <http://www.nmr-service.de/duplexer-tr-schalter.html>.
58. Mispelter, J., M. Lupu, and A. Briguet, *NMR probeheads for biophysical and biomedical experiments*. 2006, London; Hackensack, NJ: Imperial College Press; Distributed by World Scientific.
59. Schuler, K., *Hochfrequenztechnik 1 - Skript zur Vorlesung*. 2013, Institut für Hochfrequenztechnik - Hochschule Mannheim: Mannheim.
60. 9A4QV. *LNA for HF*. [cited 2016 9. Nov.]; Available from: <http://lna4hf.blogspot.de/>.
61. Pozar, D.M., *Microwave engineering*. 2012, Hoboken, NJ: Wiley.
62. Wetterling, F., *The Detection of Infarcted Stroke Tissue via Localized Sodium Concentration Measurements: A Non-Invasiv Approach*. 30.10.2009, The University of Dublin - Trinity College: Dublin. p. 199.
63. Blasiak, B., et al., *An optimized solenoidal head radiofrequency coil for low-field magnetic resonance imaging*. Magnetic Resonance Imaging, 2009. **27**(9): p. 1302–1308.
64. Klepsch, T., et al., *Calibration of fibre-optic RF E/H-field probes using a magnetic resonance (MR) compatible TEM cell and dedicated MR measurement techniques*. BMTZ, 2012. **57**(1).
65. Mouser Electronics. *BLF188XR, NXP*. [cited 2016 26. Nov.]; Available from: [http://www.mouser.com/ds/2/302/BLF188XR\\_BLF188XRS-271330.pdf](http://www.mouser.com/ds/2/302/BLF188XR_BLF188XRS-271330.pdf).
66. Blasiak, B., et al., *An optimized solenoidal head radiofrequency coil for low-field magnetic resonance imaging*, in *Magnetic Resonance Imaging*. 2009. p. 1302-1308.
67. Pure Devices GmbH. *Research Lab drive I*. 2015 [cited 2016 24. Nov.]; Available from: [http://www.pure-devices.com/images/Flyer/Research\\_Lab\\_Detailed\\_Specifications.pdf](http://www.pure-devices.com/images/Flyer/Research_Lab_Detailed_Specifications.pdf).
68. Ettus Research. *BasicTX Daugtherboard*. [cited 2016 26. Nov.]; Available from: <https://www.ettus.com/product/details/BasicTX>.
69. Ettus Research. *BasicRX Daughterboard*. [cited 2016 26. Nov.]; Available from: <https://www.ettus.com/product/details/BasicRX>.

# Appendix

Abstract submitted to the International Society for Magnetic Resonance in Medicine (ISMRM) Conference 2017 in Honolulu, Hawai'i.

## **COSI Transmit: Open Source Soft- and Hardware Transmission System for traditional and rotating MR**

Christian Blücher<sup>1</sup>, Haopeng Han<sup>1</sup>, Werner Hofmann<sup>2</sup>, Reiner Seemann<sup>2</sup>, Frank Seifert<sup>2</sup>, Thoralf Niendorf<sup>1,3,4</sup>, and Lukas Winter<sup>1</sup>

<sup>1</sup>Berlin Ultrahigh Field Facility (B.U.F.F.), Max Delbrück Center for Molecular Medicine in the Helmholtz Association, Berlin, Germany; <sup>2</sup>Physikalische Technische Bundesanstalt (PTB), Berlin, Germany; <sup>3</sup>Experimental and Clinical Research Center (ECRC), a joint cooperation between the Charité Medical Faculty and the Max Delbrück Center for Molecular Medicine, Berlin, Germany; <sup>4</sup>MRI.TOOLS GmbH, Berlin, Germany

### **Synopsis**

As part of the open source imaging initiative ([www.opensourceimaging.org](http://www.opensourceimaging.org)), a collaborative effort to build an open source MRI, we proposed and built a transmission/reception RF system mostly consisting of open source components for traditional and rotating spatial encoding schemes. COSI Transmit is based on a GNU Radio compatible software defined radio (SDR) as a spectrometer, a 1kW RF-power amplifier, T/R switch, low noise preamplifier and a transmit/receive solenoid RF coil. The system operates in the frequency range from 1.8-30MHz ( $B_0=0.042-0.7T$ ) and can potentially be extended to  $B_0=1.27T$ . Material cost of the system is ~3000€.

### **Purpose**

MRI is a crucial medical device that is beyond the reach of many patients throughout the world<sup>1</sup>. Cost effective open source imaging (COSI) is part of the open source imaging initiative (OSI<sup>2</sup>) currently building an affordable open source MRI system in order to address this issue<sup>2</sup>. Here we present COSI transmit, an open source transmission/reception system for low field ( $B_0=0.042-0.7T$ ) MRI of traditional and rotating spatial encoding schemes<sup>3</sup>. COSI transmit consists of a spectrometer, RF power amplifier (RFP), transmit/receive switch, low noise preamplifier and RF coil.

### **Methods**

A schematic of COSI transmit modules is displayed in Fig.1a.

The primary requirement for the spectrometer hardware was GNU Radio<sup>4</sup> and gr-MRI<sup>5</sup> compatibility. This approach allows hardware independent developments of imaging techniques. An USRP1<sup>6</sup> SDR ( $f=DC-6GHz$ , ADC: 12bit 64MS/s, DAC: 14bit 128MS/s) was implemented with two transmit<sup>7</sup> and one receive<sup>8</sup> daughterboard ( $f=0-30MHz$ ). We extended the gr-MRI<sup>5</sup> code utilizing GPIO pins embedded in the board allowing the use of a single SDR for stepper motor control of rotating gradient fields used for spatial encoding<sup>9,10</sup>.

A RF amplifier ( $P_{out}=1kW$  peak,  $f=1.8-54MHz$ ) was developed consisting of a driver stage, an output stage, a low pass filter, a blanking/unblanking circuit and a cooling circuit (Fig.2a). For the driver a two stage linear amplifier<sup>11</sup> (gain:33-34dB,  $P_{out}=5W$ ,  $f=1.8-150MHz$ ) and for the output stage the design of W6PQL<sup>12</sup>, a 1kW peak solid state pallet amplifier (gain:22-27dB,  $f=1.8-54MHz$ ) based on a power LDMOS transistor (BLF188XR) was chosen. A 1.5kW low pass filter<sup>12</sup> at the output suppresses unwanted harmonics. A level converter is used at the SDR output to match the TTL high for RFP unblanking. For un-/blanking the amplifier, the power supply voltage is switched on/off respectively via CMOS

transistors. In addition after 3 $\mu$ s the LDMOS source is clamped to discharge the capacities and suppress any additional RF noise of the output stage during MR signal reception.

A passive T/R-switch<sup>13</sup> (3-5MHz, 47dB isolation,  $P_{\max}=1.3\text{kW}$ ) was used to connect the RF coil and the RFPA. For MR signal pre-amplification a low noise preamplifier<sup>14</sup> is utilized ( $f=150\text{kHz}-30\text{MHz}$ , gain:18-20dB, noise figure=1-2dB).

The RF coil was constructed based on electromagnetic field simulations<sup>15</sup> for a frequency of  $f=3.63\text{MHz}$ , which is the center frequency of our prototype Halbach magnet. A solenoid design was chosen as a transmit/receive RF coil to adapt to the Halbach magnet  $B_0$  field distribution. RF coil loading was modeled by a spherical sample with 70mm diameter representing muscular tissue. The length and number of turns was adjusted to reach a homogenous  $B_1^+$  field distribution inside the sample (Fig.5c).

The simulations were validated with  $S_{12}$ -measurements<sup>16</sup> of a pickup loop positioned along a straight line at one end of the RF coil.  $B_1$  calibration of the pickup loop was done in a known B-field of a TEM-cell<sup>17</sup> (Fig.5a,b,d). This approach allows for a low cost validation of the EM fields at such low frequencies without using more expensive E- or H-field sensors.

## **Results**

The spectrometer is capable of producing arbitrary shaped RF-pulses, un-/blanking the RFPA, recording acquired data and controlling rotating gradient fields (Fig.1c). Pulse length, amplitude, readout-length and –delay can be chosen freely.

The RFPA successfully amplified rect- and sinc-pulses generated by the spectrometer (Fig.3b,d). A signal amplitude of 500mV at the input leads to an output voltage level of 200V which corresponds to a total gain factor of 52dB and a power level of 800W in a 50 $\Omega$  system (Fig.3). The expected distortions observed (Fig. 3) will be addressed by digital predistortion techniques. The RFPA shows good linearity for the investigated frequency range  $f=1.8-54\text{MHz}$  ( $B_0=0.042-1.27\text{T}$ ) with a maximum power output of around 1kW peak power (Fig.4).

The RF coil consists of  $N=20$  windings, length=200mm and radius=48mm (Fig.5d). The measured Q-factors are  $Q_{\text{loaded}}=155$  and  $Q_{\text{unloaded}}=189$ . Simulated  $B_1^+$  amplitude in the RF coil center is  $\sim 2694\mu\text{T}/\sqrt{\text{kW}}$  with a  $B_1^+$ -field inhomogeneity within the sample  $<3.4\%$  (Fig. 5c). The mean difference between validation measurements and simulations was  $-5.1\pm 4.2\%$  for absolute and  $1.2\pm 4.5\%$  for relative values. The whole system occupies a volume of around  $(50\times 30\times 35)\text{cm}^3$ . The total cost of the system is  $\sim 3000\text{€}$  (SDR:1000€; RFPA:1500€; T/R-Switch:370€; LNA:20€; RF-coil:100€).

## **Conclusion**

An affordable ( $\sim 3000\text{€}$ ) MR transmission/reception system was developed by using mainly open source hardware components. In its current configuration COSY transmit can be used for  $B_0=0.042-0.7\text{T}$  (extendable to 1.27T) MRI systems with traditional and rotational spatial encoding schemes. Technical documentation of the system will be made available at [www.opensourceimaging.org](http://www.opensourceimaging.org) according to the principles of open source hardware. Further work will focus on developing a fully open source spectrometer, T/R switch and RFPA module allowing to improve the performance and lowering costs.

## **Acknowledgements**

The authors would like to express their gratitude to Christopher J. Hasselwander and William A. Grissom for helpful assistance in gr-MRI.

## **References**

- <sup>1</sup> World Health Organization, "Global Health Observatory (GHO) data: Medical equipment (density per million population)", 2014
- <sup>2</sup> Winter L, et. al., ISMRM, 2016, #3638
- <sup>3</sup> Cooley CZ, et al., MRM, 2015; 73(2):872-83
- <sup>4</sup> GNU Radio, <http://gnuradio.org/>
- <sup>5</sup> Hasselwander C.J., et al., JMR, 2016;270:47:55
- <sup>6</sup> USRP1, Ettus Research, Mountain View, USA
- <sup>7</sup> LFTX daughterboard (0-30MHz), Ettus Research, Mountain View, USA
- <sup>8</sup> LFRX daughterboard (0-30MHz), Ettus Research, Mountain View, USA
- <sup>9</sup> Winter L, et al. ISMRM, 2015, #3568
- <sup>10</sup> Blümmler P, Conc Magn Reson Part B: Magn Reson Eng, vol. 46, pp. 41-48, 2016.
- <sup>11</sup> Funkamateur, Bausatz für QRP-Linear-Endstufe, DL2EWN, <http://www.box73.de/>
- <sup>12</sup> W6PQL, <http://www.w6pql.com/1kwsspafor18-54mhz.htm>
- <sup>13</sup> NMR Service GmbH, Erfurt, Germany
- <sup>14</sup> LNA4HF, 9A4QV, <http://lna4hf.blogspot.de/>
- <sup>15</sup> CST MWS 2012, Darmstadt, Germany
- <sup>16</sup> Spectrum analyzer, Rohde & Schwarz, München, Germany
- <sup>17</sup> Klepsch T., et al., BMT, 2012; 57(1)

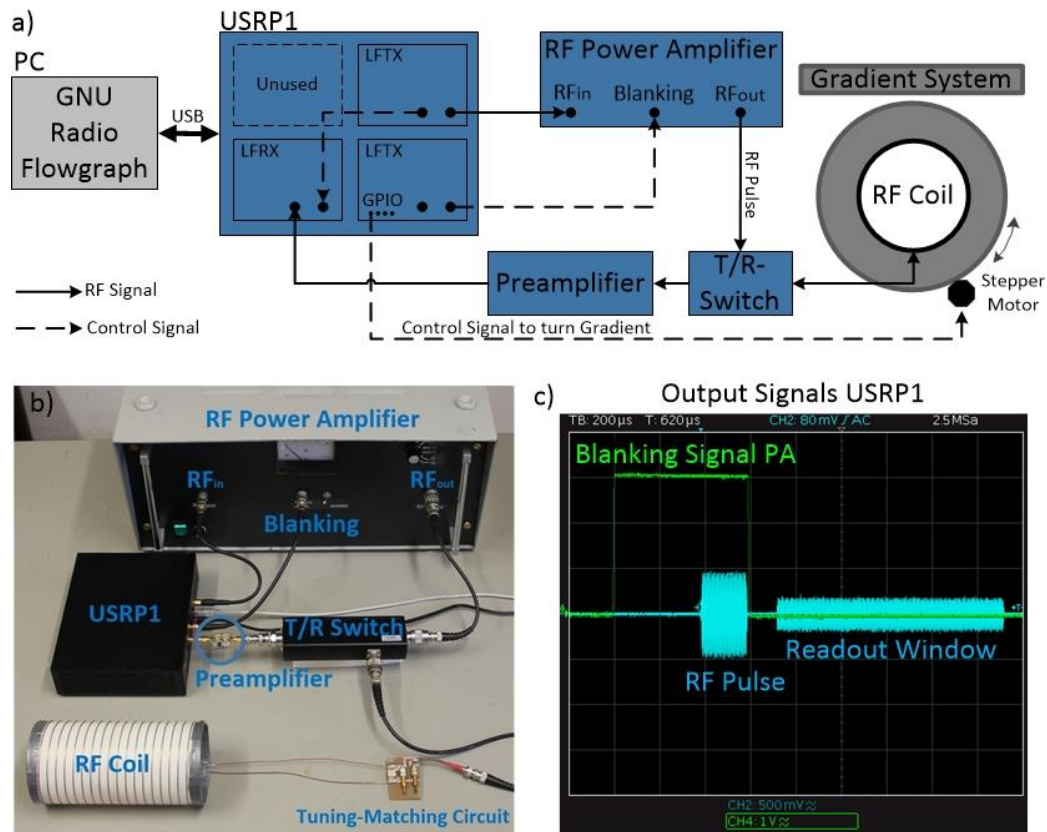


Figure 1 – Schematic (a) and photograph (b) of COSY transmit: GNU Radio flowgraph runs on a computer, controls and communicates with USRP1 via USB. The LFTX daughterboards generate the RF-pulse, blanking signal and readout window (c). Data acquisition is synchronized to the transmission by feeding back the readout window signal to the LFRX receive-board. The RPA amplifies the RF-pulse, which is sent to the TX/RX-RF coil via T/R-switch. The received signal is amplified with an LNA and digitized on the LFRX-board. GPIO pins on the LFTX-board are used to control a stepper motor driving circuit for gradient system rotation.



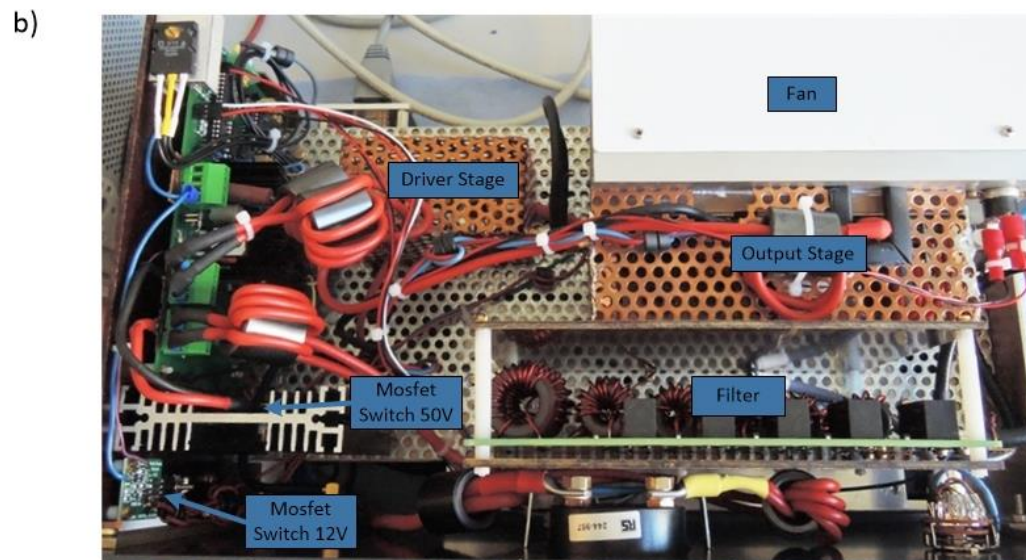
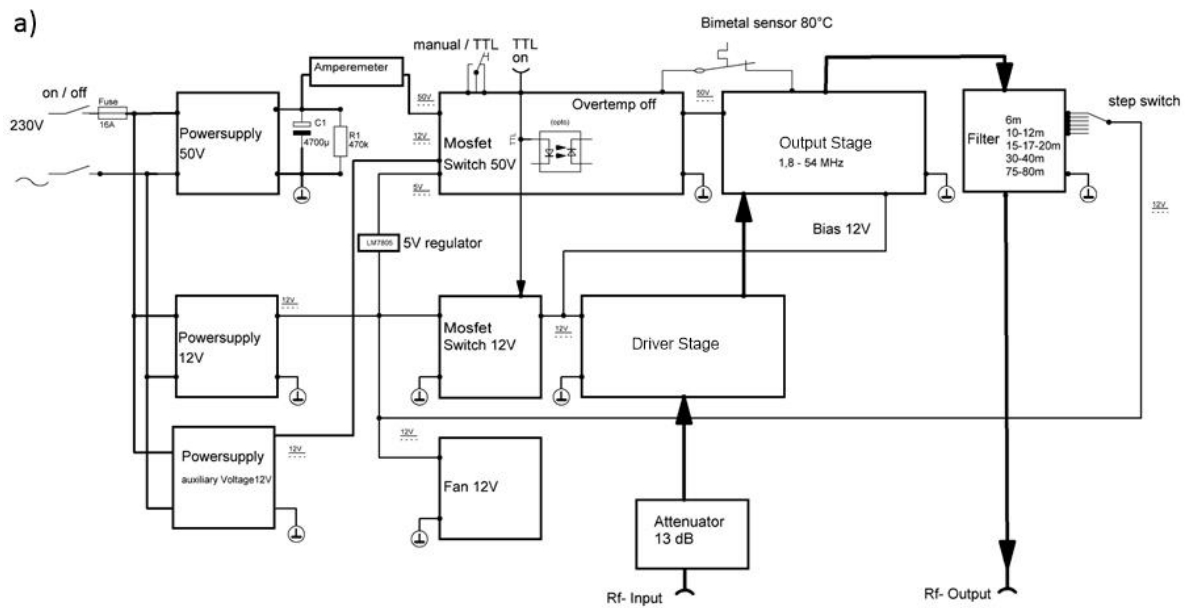


Figure 2 – Schematic (a) and photograph (b) of the RF-power-amplifier: The RFPA consist of a driver stage (Gain=33-34 dB) and an output stage (Gain=22-27dB, Pout=1kW). The adjustable low pass filter at the output suppresses unwanted harmonics. To blank/unblank the amplifier, the 12V and 50V power supplies are connected and disconnected to the amplification stages respectively using CMOS transistors.

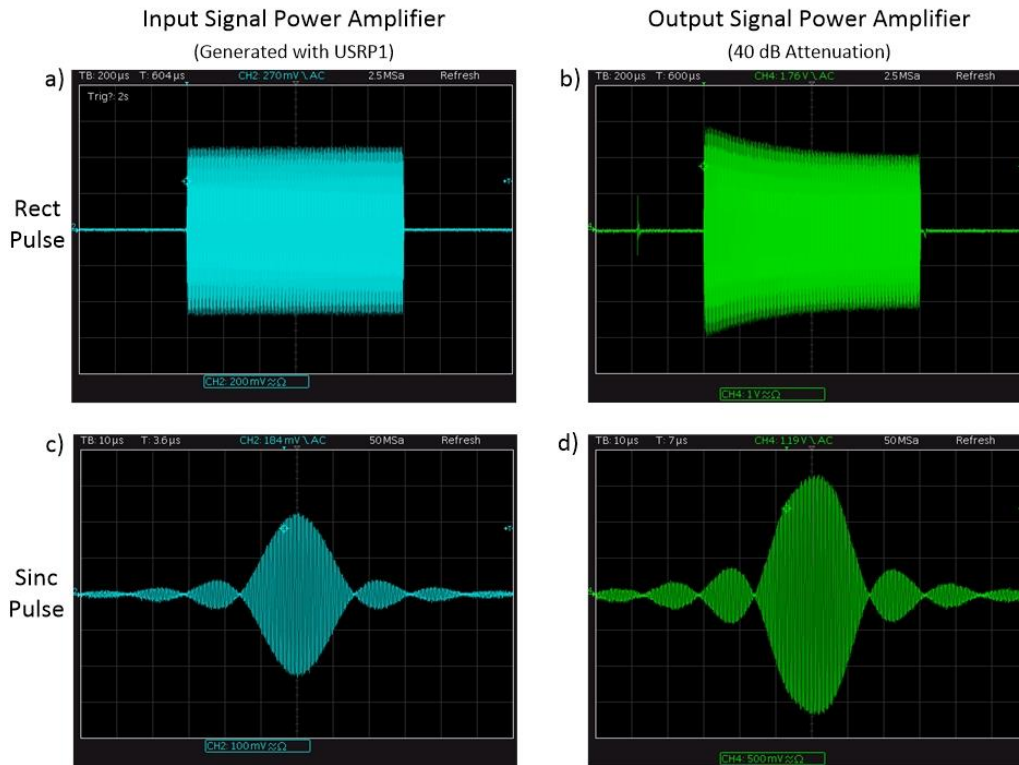


Figure 3 – 1200  $\mu$ s long rect pulse with an amplitude of 500mV (a) and a 120 $\mu$ s long sinc pulse with a maximum amplitude of 200mV (c) are shown on the left side. Both pulses are generated by the SDR spectrometer. On the right side (b,d) the same pulses are shown after amplification with the RF-power amplifier and 40dB attenuation. The expected distortions observed will be addressed by digital predistortion techniques.

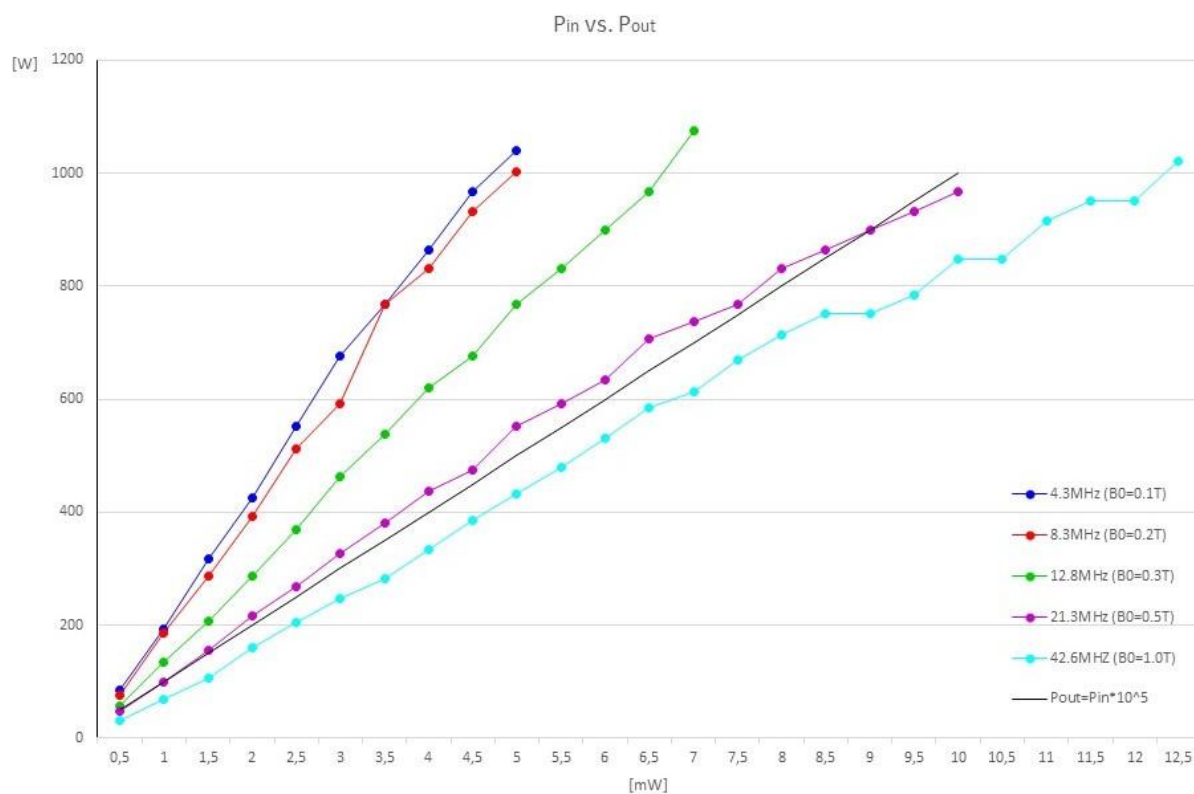


Figure 4 – Input power  $P_{in}$  plot versus the output power  $P_{out}$  of the RFPA for the Larmor frequencies of hydrogen at magnetic field strengths  $B_0=0.1T, 0.2T, 0.3T, 0.5T$  and  $1.0T$  showing good linearity over the investigated frequency range.

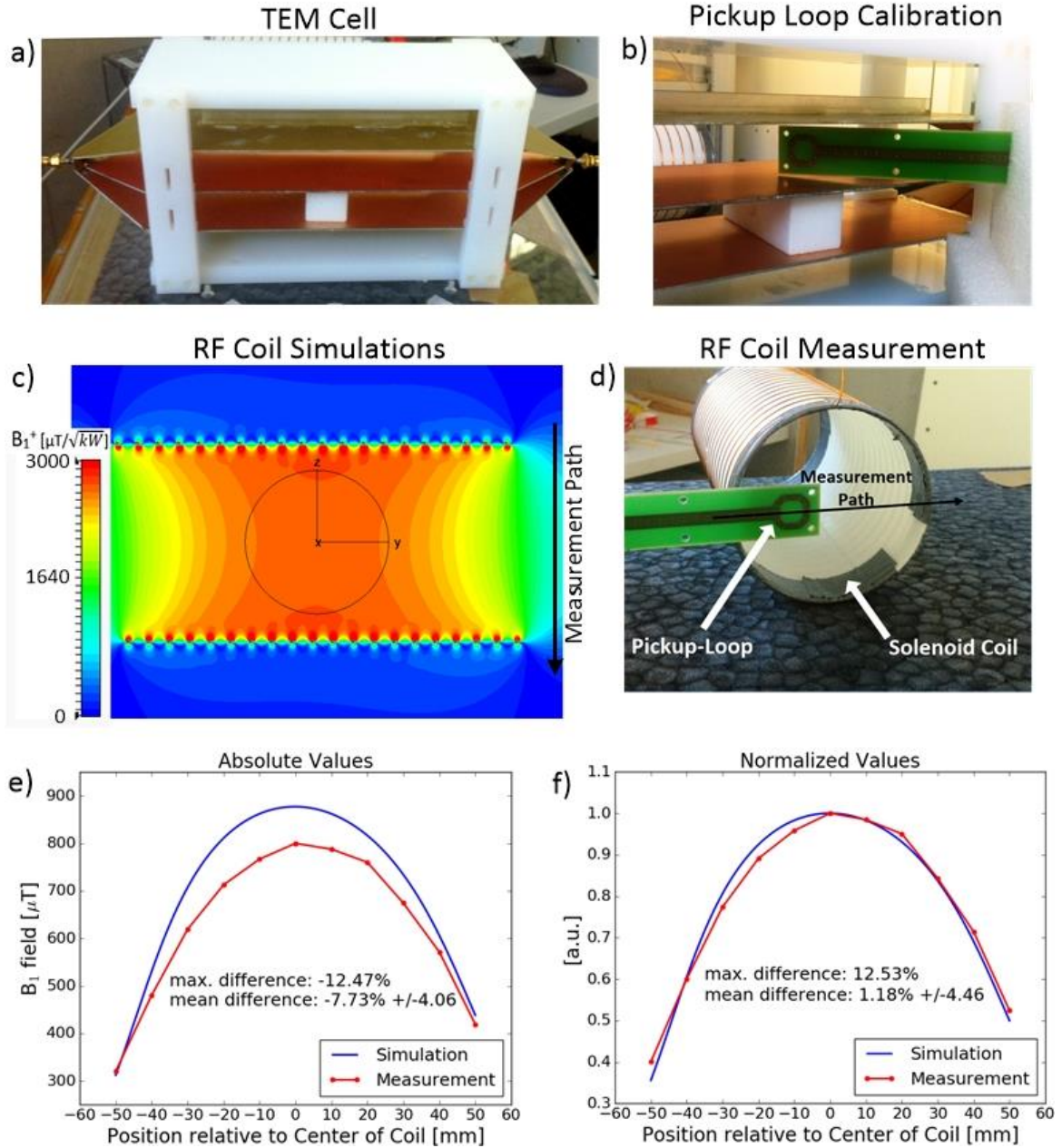


Figure 5 –  $B_1^+$  measurement setup of the solenoid RF coil and comparison to the EMF simulations. a) TEM cell with known B field distribution b) Pickup loop calibration with the spectrum analyzer. c) Simulated  $B_1^+$  field distribution of the solenoid coil and measurement path position. d) Pickup loop measurements along a straight line at the end of the RF coil. e) Absolute and f) normalized comparison of simulated and measurement  $B_1^+$  values of the RF coil.